ORNL/SPR-2022/2707
CRADA/NFE-21-08507

Extend an innovative HPC-Compatible Multiple Temporal-spatial Resolution Concurrent Finite Element Modeling Approach to Guide Laser Powder Bed Fusion Additive

Xiaohua Hu
Jiahao Cheng
Mei Li (Ford)
Yang Huo (Ford)
Yang Li (Ford)
Bita Ghaffari (Ford)
Joy Forsmark (Ford)
Eric Poczatek (Ford)

11/21/2022

OAK RIDGE NATIONAL LABORATORY
MANAGED BY UT-BATTELLE FOR THE US DEPARTMENT OF ENERGY

DOCUMENT AVAILABILITY

Reports produced after January 1, 1996, are generally available free via US Department of Energy (DOE) SciTech Connect.

Website http://www.osti.gov/scitech/

Reports produced before January 1, 1996, may be purchased by members of the public from the following source:

National Technical Information Service
5285 Port Royal Road
Springfield, VA 22161
Telephone 703-605-6000 (1-800-553-6847)
TDD 703-487-4639
Fax 703-605-6900
E-mail info@ntis.gov
Website http://www.ntis.gov/help/ordermethods.aspx

Reports are available to DOE employees, DOE contractors, Energy Technology Data Exchange representatives, and International Nuclear Information System representatives from the following source:

Office of Scientific and Technical Information
PO Box 62
Oak Ridge, TN 37831
Telephone 865-576-8401
Fax 865-576-5728
E-mail reports@osti.gov
Website http://www.osti.gov/contact.html

This report was prepared as an account of work sponsored by an agency of the United States Government. Neither the United States Government nor any agency thereof, nor any of their employees, makes any warranty, express or implied, or assumes any legal liability or responsibility for the accuracy, completeness, or usefulness of any information, apparatus, product, or process disclosed, or represents that its use would not infringe privately owned rights. Reference herein to any specific commercial product, process, or service by trade name, trademark, manufacturer, or otherwise, does not necessarily constitute or imply its endorsement, recommendation, or favoring by the United States Government or any agency thereof. The views and opinions of authors expressed herein do not necessarily state or reflect those of the United States Government or any agency thereof.

ORNL/SPR-2022/2707
CRADA/ NFE-21-08507

Division or Program Name

Extend an innovative HPC-Compatible Multiple Temporal-spatial Resolution Concurrent Finite Element Modeling Approach to Guide Laser Powder Bed Fusion Additive

Xiaohua Hu
Jiahao Cheng
Mei Li (Ford)
Yang Huo (Ford)
Yang Li (Ford)
Bita Ghaffari (Ford)
Joy Forsmark (Ford)
Eric Poczatek (Ford)

Date Published:

July 18, 2023

Prepared by
OAK RIDGE NATIONAL LABORATORY
Oak Ridge, Tennessee 37831-6283
managed by
UT-BATTELLE, LLC
for the
US DEPARTMENT OF ENERGY
under contract DE-AC05-00OR22725

1. Abstract

Laser power bed fusing (PBF) additive manufacturing is a key enabling technology to manufacture highly complex and integrated automotive structures. However, the geometric complexity of PBF-AM technique also leads to highly non-uniform heating and cooling rate in the manufactured part, which may cause flaw formation and produce excessive and nonuniform residual stresses, which increase quality uncertainties and manufacture issues, leading to increases in cost and energy consumption in the form of rejected parts. In this research project, we developed an innovative Multi-Spatial-Temporal-Resolution Finite Element (MUST-FE) method and completed the corresponding high performance computation (HPC) platform-based in-house code, which enables high accuracy prediction of temperature and residual stress fields for component-scale PBF-AM manufacture in efficient computation time. The MUST-FE model is calibrated and validated with a “2D pad” AlSi10Mg experiments by matching the melt pool shape and dimension, and with a “XY-cross” AlSi10Mg experiment by matching the thermal distortion and residual stress. . The innovative multi-resolution and concurrent modeling approach adopted in this code ensures accuracy and computational efficiency, which will enable energy-efficient and high-yield, low-cost manufacturing of optimized, qualifiable automotive structures and contribute towards reaching technical targets outlined in AMO’s Program Plan to develop additive manufacturing systems that deliver consistently reliable parts with predictable properties.

2. Statement of Objectives

The technical scope of this work is to develop and validate a fully coupled thermo-mechanical HPC-FE AM code based on the MUST-FE approach, which can predict residual stresses and resultant distortions for L-BPF with higher accuracy and computation efficiency, compared to current commercial software and academic codes. The objective is to utilize this advance HPC-FE code to virtually screen and optimize process parameters to ensure the quality of AM products by minimizing the magnitude of deleterious residual stress and unwanted geometrical distortions.

The task plan includes both HPC development and experimental validation. ORNL team will focus on modeling development, including extending the current pseudo-3D code to full-3D, then followed by modifying the code to represent the additive nature of AM. Once modified, an advanced computational efficient wavelet-based FE solver[21] will be utilized to optimize the computational efficiency. Finally, the developed code will be tested in the ORNL HPC facilities (CADES) and then used to perform L-PBF process simulations for AlSi10Mg X-Y asymmetry demo-samples. The validation plan will be completed collaboratively between the Ford and ORNL teams, including single-track experiments to calibrate MUST-FE code to have reasonable predication at melting pool scale and print of demo-samples to test 3 level MUST-FE code at part scale.

Advances the current state of the art in the industrial sector: The current multi-resolution concurrent modeling (MUST-FE) scheme will be a significant advancement of the current state of art in modeling additive manufacturing and acceleration of the usage of AM in the US advanced manufacturing industry in the following aspects:

- Fully coupled between thermal and mechanical fields, eliminating inaccurate thermal distortion predictions due to fields mismatch;
- Enabling multi-resolution discretization not only in the in-plane directions on current layer, but also in AM building (thickness) direction. Such feature is achieved by having the fine FE model moving inside the coarser FE domain following the laser track. This will allow direct simulation of

the entire building process instead of using ad-hoc scaling up approach.

- Enabling adaptive time integration with fine time increments on fast evolution region and large time increments on the slow evolving regions, avoiding wasting computation cost on most regions of the part that evolve slowly in temperature and stress. This can provide an estimated acceleration in computational speed by a factor of 100~1000×.
- The use of a-priori constructed multi-resolution meshes, avoids frequent remeshing and the associated FE matrix re-assembling in state-of-art methods, which translates into significant computational costs.
- MUST-FE model has better HPC parallelization efficiency since the multi FE models at different resolution can be executed in parallel on multi-cores.

This code can impact the US advanced manufacturing sector by delivering accurate models to minimize deleterious residual stresses, thus increasing the reliability and durability of AM components. With the help of HPC, the code can deliver extra-fast simulations to make it possible to accelerate the design-development-deployment cycle of complex components, thus strengthening the competitive advantage of US manufacturing.

3. Benefits to the Funding DOE Office's Mission

This project will benefit the U.S. Department of Energy Advanced Materials & Manufacturing Technology office mission of developing additive manufacturing systems that deliver consistently reliable parts with predictable properties

4. Technical Discussion of the Work Performed by All Parties

In order to most effectively and efficiently meet the project objectives outlined above, the team established a project plan with five tasks

1) Collect Thermal Properties and Mechanical Properties for Al10SiMg Powder Materials Model testing and validation
2) Extend the Current Pseudo-3D MUST-FE code into Full 3D and Validate this Full 3D MUST-FE code using Single-track Experiments
3) Conduct Simulations for X-Y Asymmetry Demo-samples on HPC using the 3D MUST-FE code.
4) Print X-Y Asymmetric Demo-samples using Selected Process Parameters and Characterize Residual Stress and Distortion for Model Validation at part Scale.
5) Benchmark and Component Demonstration

4.1 Collect Thermal Properties and Mechanical Properties for Al10SiMg Powder Materials Model testing and validation

The elements for the base and the powder layer are assigned to two different sets of material properties (bulk AlSi10Mg and powder AlSi10Mg), as listed in table 2.

Table 1. Thermal properties of AlSi10Mg [1]

Temperature (K)	298	473	673	820	870	1000
Density (bulk) (kg/m^3)	2650	2550	2400	2200	2000	1900
Thermal conductivity (bulk) ($W/(mK)$)	147	159	159	159	100	105
Specific heat capacity (bulk) ($J/(kg\ K)$)	739	797	838	922	1100	1000
Density (powder) (kg/m^3)	920	930	950	1000	-	-
Thermal conductivity (powder) ($W/(mK)$)	1.5	1.6	1.7	1.8	-	-
Specific heat capacity (powder) ($J/(kg\ K)$)	443	478	503	553	-	-

4.2 Extend the Current Pseudo-3D MUST-FE code into Full 3D and Validate this Full 3D MUST-FE code using Single-track Experiments

4.2.1 Overview of MUST-FE method

The MUST-FE is a method that computes the thermal and mechanical fields for large geometrical model with fine local resolution that is necessary to resolve local melt pool. It is composed of multi-level sub-domain FE meshes, as illustrated in Figure 1. In Figure 1a, a two-levels MUST-FE model is demonstrated. The coarse model is designed to be large enough to capture the geometry of the entire powder bed, while the sub-model has very fine mesh resolution to capture the laser-induced melt pool. While the coarse model is fixed spatially, the fine sub-model moves following the moving of laser. The two-level models are solved using an iterative algorithm, in which each level is solved as a separate FE problem while the resulted temperature and displacement fields are passed to the other levels as heat input and constraining boundary conditions. The mesh at each sub-domain level is "de-attached" from other levels in the sense that the nodes at each level do not form element-connectivity, and the finer-level mesh can move freely in the coarser mesh domain. This feature is in contrast to the adaptive mesh-refinement FE method (h-FEM) or remeshing-based FE method in which the refined mesh region and coarse mesh region are solved together by forming one large FE matrix. The MUST-FE methods allows construction of arbitrary number (≥ 2) of levels sub-models, as illustrated in Figure 1b (two-dimensional) and 1c (three-dimensional), respectively. When applied to L-PBF process, the hierarchy of MUST-FE framework can be design to assign specific features on each level, which is illustrated in Figure 2 and explained in details in section 4.3.

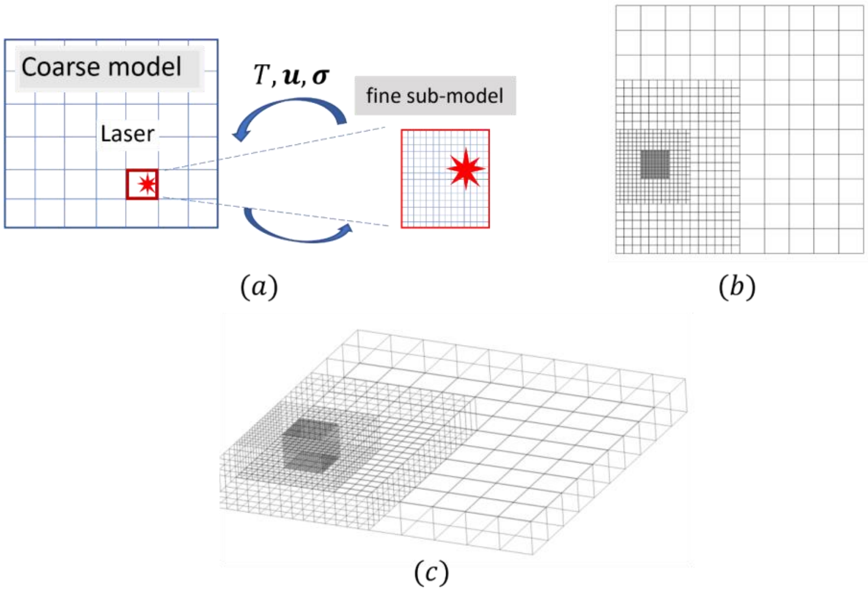

Fig 1. Illustration of a MUST-FE model, the model is constructed with multi-level sub-domain meshes. (a) illustration of forming a MUST-FE problem with two levels. (b) a two-dimensional four-levels MUST-FE model. (c) a three-dimensional four-levels MUST-FE model

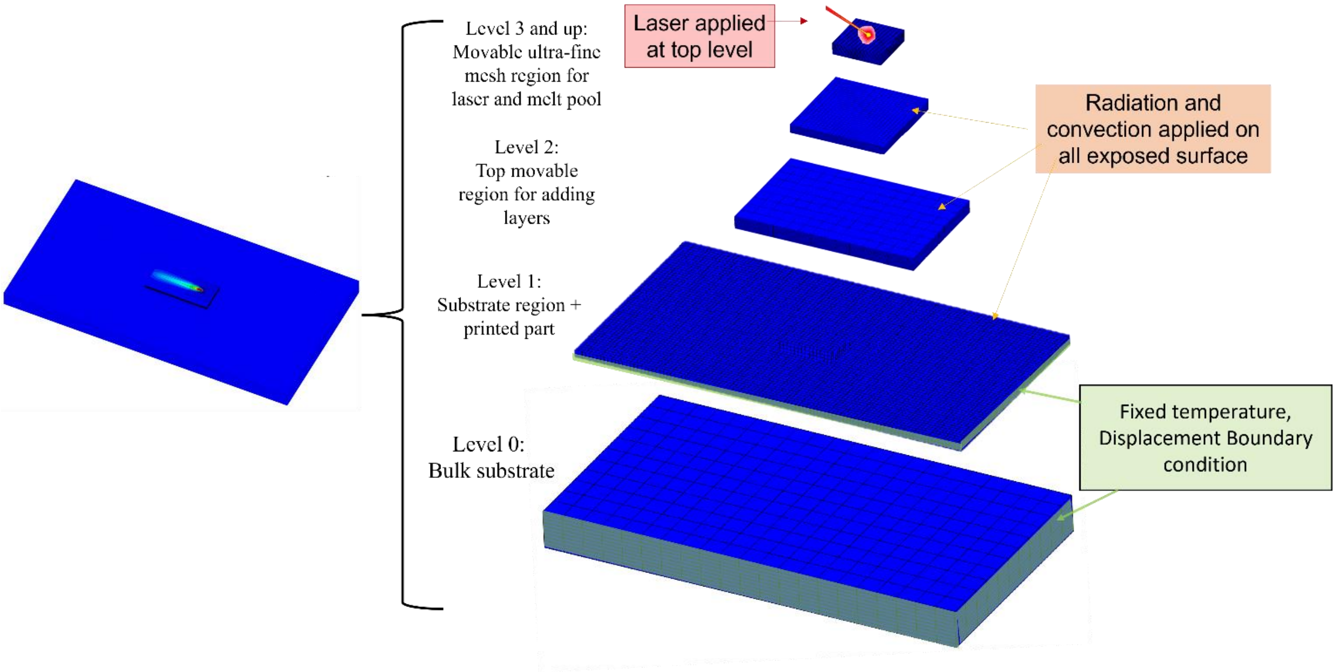

Fig 2. Illustration of the hierarchy of a 5 levels MUST-FE model design specially for L-PBF simulation. The details are given in section 4.3.

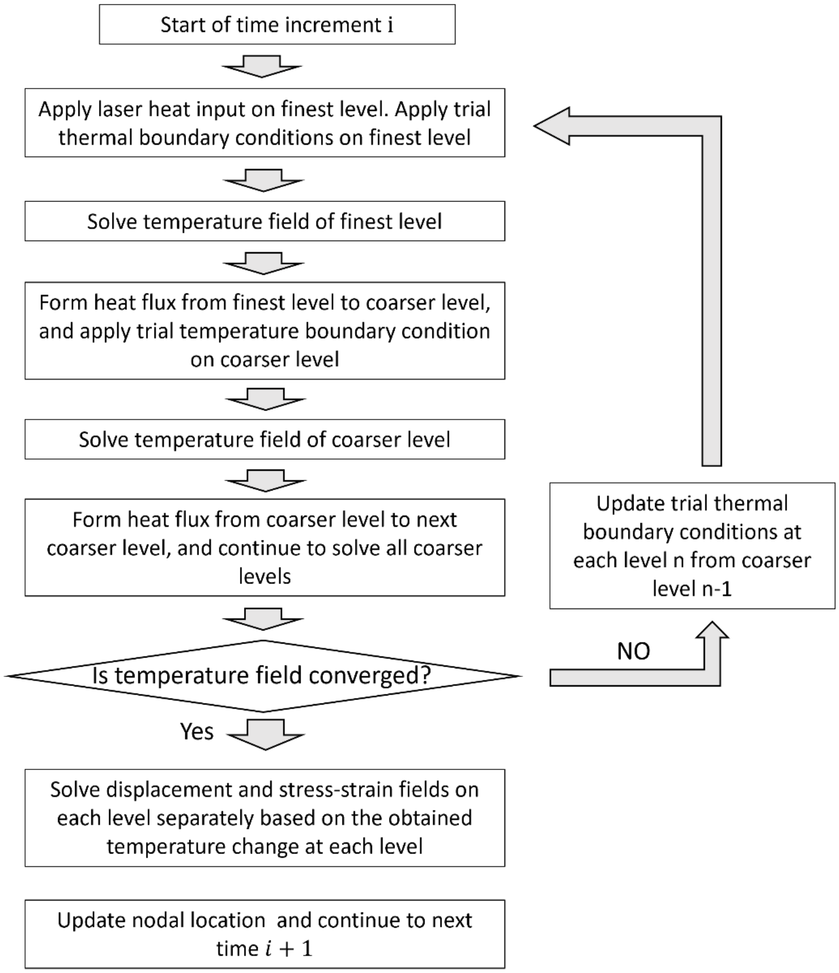

Fig 3. Overview of MUST-FE method solving algorithm.

The general numerical solving algorithm of MUST-FE method is shown in Figure 3. The MUST-FE methods solves both temperature field and deformation fields (displacement, stress, elastic and plastic strain) in a stagger-coupled approach. In the following section 4.2.2-4.2.7, the thermal part of MUST-FE method is described in details with experiment calibration and validation process, while the mechanical part and thermal-mechanical coupling is described in section 4.2.8-4.2.9.

4.2.2 numerical formulation of MUST-FE method

At each sub-domain, the thermal and mechanical fields are solved using the staggered algorithm in Fig. 3. The to-be-solved thermal problem is governed by the following heat transfer equation:

$$\rho C \frac{\partial T}{\partial t} = \frac{\partial}{\partial \boldsymbol{x}}\left(\boldsymbol{k}\frac{\partial T}{\partial \boldsymbol{x}}\right) + \rho P_{laser} + P_c + P_r + Q \tag{1}$$

Where T is the to-be-solved temperature at a material point, ρ is material density, C is temperature dependent material specific heat, $\boldsymbol{k}$ is the temperature-dependent thermal conductivity matrix,

P_{laser} is the input heat flux from laser, P_c and P_r are the heat flux due to material surface thermal convection and radiation, which are expressed as

$$P_c = -\int h_c(T - T_0)d\Gamma \tag{2}$$

$$P_r = -\int \varepsilon\sigma(T^4 - T_0^4)d\Gamma \tag{3}$$

Where T_0 is the ambient temperature, Γ is the material surface region. Q in equation (1) is the internal heat generation, e.g., due to material phase change. The FE method solves the variational weak form of equation (1) which is obtained from Galerkin method and by applying FE shape functions to approximate the temperature [Bathe]. By using an implicit forward Eulerian time integration algorithm, the weak form equation in FE matrix form is expressed as:

$$\boldsymbol{C}\left(\frac{\boldsymbol{T}^{t+\Delta t} - \boldsymbol{T}^{t}}{\Delta t}\right) + \boldsymbol{K}\boldsymbol{T}^{t+\Delta t} + \boldsymbol{K}_c\boldsymbol{T}^{t+\Delta t} + \boldsymbol{K}_r\boldsymbol{T}^{t+\Delta t} = \boldsymbol{P}_{laser} + \boldsymbol{P}_c + \boldsymbol{P}_r + \boldsymbol{Q} \tag{4}$$

Where$\boldsymbol{T}^t$ and $\boldsymbol{T}^{t+\Delta t}$ are the nodal temperature vectors at time t and $t + \Delta t$, respectively. $\boldsymbol{C}, \boldsymbol{K}, \boldsymbol{K_c}, \boldsymbol{K_r}$, $\boldsymbol{P}_{laser}, \boldsymbol{P}_c, \boldsymbol{P_r}, \boldsymbol{Q}$ are respectively expressed as:

$$\boldsymbol{C} = \sum_e \int_{\Omega^e} \rho C \boldsymbol{N}^T \boldsymbol{N} d\Omega^e \tag{5}$$

$$\boldsymbol{K} = \sum_e \int_{\Omega^e} \boldsymbol{B}^T \boldsymbol{k} \boldsymbol{B} d\Omega^e \tag{6}$$

$$\boldsymbol{K}_c = \sum_e \int_{\Gamma^e} \boldsymbol{N}^T h_c \boldsymbol{N} d\Gamma^e \tag{7}$$

$$\boldsymbol{K_r} = \sum_e \int_{\Gamma^e} \boldsymbol{N}^T \varepsilon\sigma(T^2 + T_0^2)(T + T_0)\boldsymbol{N} d\Gamma^e \tag{8}$$

$$\boldsymbol{Q} = \sum_e \int_{\Omega^e} \rho C \boldsymbol{N}^T Q^e d\Omega^e \tag{9}$$

$$\boldsymbol{P}_{laser} = \sum_e \int_{\Omega^e} \boldsymbol{N}^T \rho P_{laser} d\Omega^e \tag{10}$$

$$\boldsymbol{P}_r = \sum_e \int_{\Gamma^e} \boldsymbol{N}^T \varepsilon\sigma(T^2 + T_0^2)(T + T_0)T_0 \, d\Gamma^e \tag{11}$$

$$\boldsymbol{P}_c = \sum_e \int_{\Gamma^e} \boldsymbol{N}^T h_c T_0 \, d\Gamma^e \tag{12}$$

The nodal temperature is computed as:

$$\boldsymbol{T}^{t+\Delta t} = (\boldsymbol{C} + \Delta t\boldsymbol{K} + \Delta t\boldsymbol{K}_c + \Delta t\boldsymbol{K}_r)^{-1}(\boldsymbol{C}T^t + \Delta t\boldsymbol{P}_{laser} + \Delta t\boldsymbol{P}_c + \Delta t\boldsymbol{P}_r + \Delta t\boldsymbol{Q}) \tag{13}$$

The sparse linear equations in equation (13) are solved using the parallel version of Krylov iterative solver in PETSc (Portable, Extensible Toolkit for Scientific Computation) package [PETsc].

4.2.3 Interchanging thermal boundary conditions between different level Sub-models

In the MUST-FE method, the finest level is designed to have the spatial and temporal resolution to resolve the laser beam heat input and melt pool evolution. Accordingly, the finest level sub-domain FE problem is solved first, then the resulted heat flux is passed down to the coarser sub-domain as input. That is, for the coarser level sub-domain FE model, the $\boldsymbol{P}_{laser}$ term in equation (13) is replaced by $\boldsymbol{P}_{f\to c}$ which is the heat flux vector passed from finer level. Assuming a total of n levels are used within MUST-FE framework in a specific problem, and assume for the time increment $t \to t + \Delta t$, the sub-model at finer level i+1 is already solved and the sub-model of coarser level i is to-be-solved, the $\boldsymbol{P}_{f\to c}$ for level i sub-model is expressed as:

$$\boldsymbol{P}_{f\to c} = \boldsymbol{C}_i\left(a_{f\to \boldsymbol{c}}\boldsymbol{T}_{i+1}^{t+\Delta t} + (1 - a_{f\to \boldsymbol{c}})\boldsymbol{T}_{i+1}^{t} - \boldsymbol{T}_i^t\right) \tag{14}$$

Where $\boldsymbol{C}_i$ is the specific heat matrix at level i, $\boldsymbol{T}_{i+1}^{t+\Delta t}$is the vector containing the nodal temperature obtained from level i+1 model at overlapping nodes locations at time t+Δt, and time t, $\boldsymbol{T}_{i+1}^{t}$ is the vector containing the nodal temperature obtained from level i+1 model at overlapping nodes location at time t, and $\boldsymbol{T}_i^t$ is the vector containing nodal temperature at level i model at overlapping nodes location at time t. $a_{f\to \boldsymbol{c}}$ is a controlling constant parameter. Figure 4 demonstrates the correspondence of $\boldsymbol{T}_{i+1}^{t+\Delta t}$, $\boldsymbol{T}_{i+1}^{t}$ and $\boldsymbol{T}_i^t$ to the nodal locations.

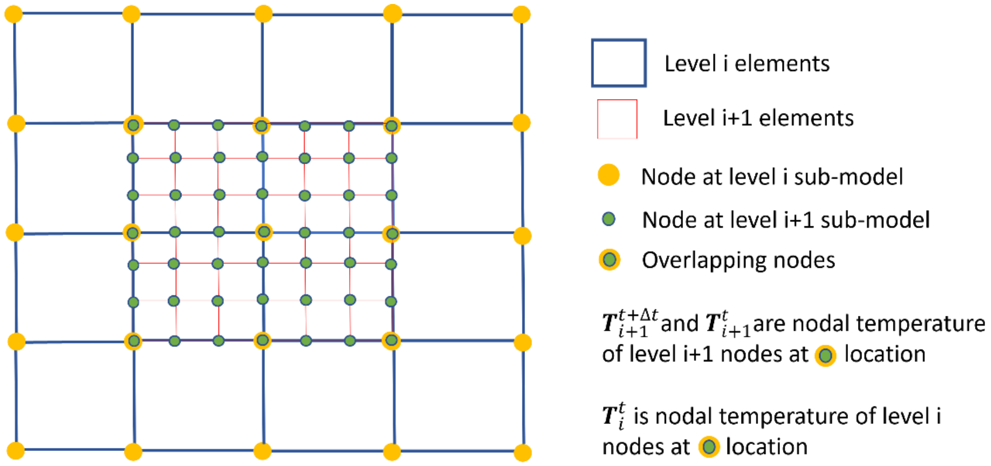

Fig. 4. Demonstration of $\boldsymbol{T}_{i+1}^{t+\Delta t}$, $\boldsymbol{T}_{i+1}^{t}$ and $\boldsymbol{T}_i^t$ in the formation of interchanging heat flux from fine to coarse level sub-models.

In addition to the heat flux, the coarse sub-model at level i also constrains the solution of fine sub-model at level i+1 by specifying the nodal temperature boundary conditions at the fine-coarse sub-model interfaces. For each interface node that at in level i+1 sub-model (see figure 5 for illustration), its nodal temperature of level i+1 is specified from the level i sub-model and expressed as:

$$T_{i+1,k}^{t+\Delta t} = \sum_{l=1,n_i} N_{i,l}(\hat{\boldsymbol{x}})T_{i,l}^{t+\Delta t} \tag{15}$$

where $T_{i+1,k}^{t+\Delta t}$ is the temperature boundary condition of a fine-coarse interface node k at level i+1, $\hat{\boldsymbol{x}}$ is the coordinates of the node k, $N_{i,l}$ is the shape function value at $\hat{\boldsymbol{x}}$ associated with a node l at level i and $T_{i,l}^{t+\Delta t}$ is the temperature of node l at level i at time $t + \Delta t$. n_i is the number of level i nodes that is spatially related to the node k at level i+1, i.e., the nodes of the level i element that the level i+1 element k is located at.

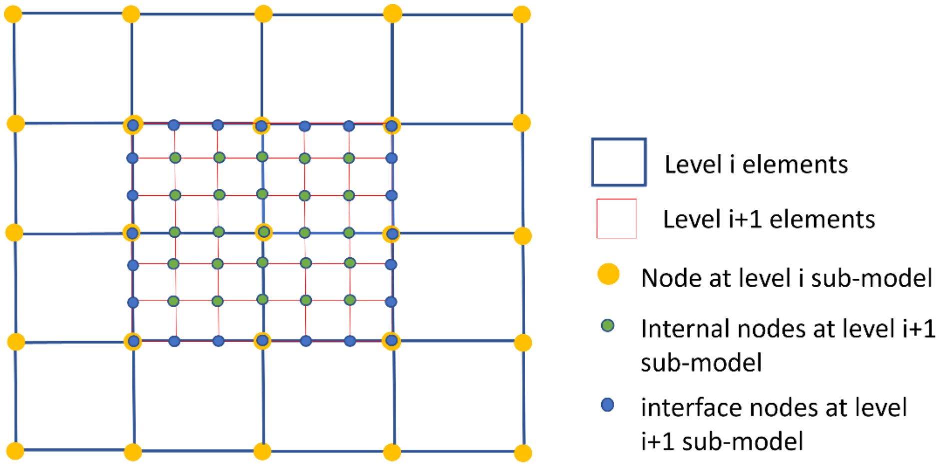

Fig. 5. Demonstration of fine-coarse interface nodes for assignment of multi-level boundary conditions.

It is noted that the level i+1 sub-model temperature is solved before level i sub-model during the iteration, and thus $T_{i,l}^{t+\Delta t}$ is not known when solving for $T_{i+1,k}^{t+\Delta t}$. Therefore, the $T_{i,l}^{t+\Delta t}$ from previous iteration (see figure 4) is used in a predicter-corrector approach.

4.2.4 Moving and remapping of sub-domains

In MUST-FE method, the location of fine sub-model is not fixed and moves following the moving of laser. This feature is demonstrated in this section using a two levels example, as shown in figure 6. In this example, the size of fine sub-model is designed to correspond to the area of 3×3 coarse elements, and the side of each fine sub-model element is ½ of the coarse element side, for the easy of demonstration. At time step $t1$, the laser is located at the coarse sub-model element (i, j), and the fine sub-model is located at the 3×3 coarse elements around (i, j), i.e., coarse element (i$\pm 0/1$, j$\pm 0/1$) & (i, j). At time step $t2$, the laser moves to coarse element (i+1, j), and the fine sub-domain is moved to the location of 3×3 coarse elements around (i+1, j), i.e., coarse element (i$+0/1/2$, j$\pm 0/1$). Note the moving of fine-domain is designed to occur at the beginning of entering time step $t2$ before the solving of FE equations for the solution of time step $t2$. A algorithm show the detailed solving order of a MUST-FE time step is shown in Figure 7. The moving of fine domain is performed by updating the node coordinates of fine sub-model nodes, and also updating the temperature and material properties of fine sub-model elements to the new locations based on the distributed value at end of time step $t1$. This updating is done in one of the two ways:

1) For the fine elements located at coarse element (i+0/1, j$\pm 0/1$) (marked in blue color in Figure 6a and 6b), their temperature and properties distribution are directly mapped from the fine sub-model nodes and elements at the same global location (but with different fine node and element indices) .
2) For the fine elements located at coarse element (i+2, j$\pm 0/1$), their nodal temperature and elemental properties are mapped from the coarse model nodes and elements at the corresponding location using the coarse shape function-based projection.

It is noted that in the case the laser scan strategy is not a continuous trajectory and involves jumping, the fine sub-model domain at new laser location at time step $t2$ is likely to have no overlapping region with the region at time step $t1$, and in that case all fine sub-domain nodal and elemental updates are mapped from the coarse model, i.e., following the method 2).

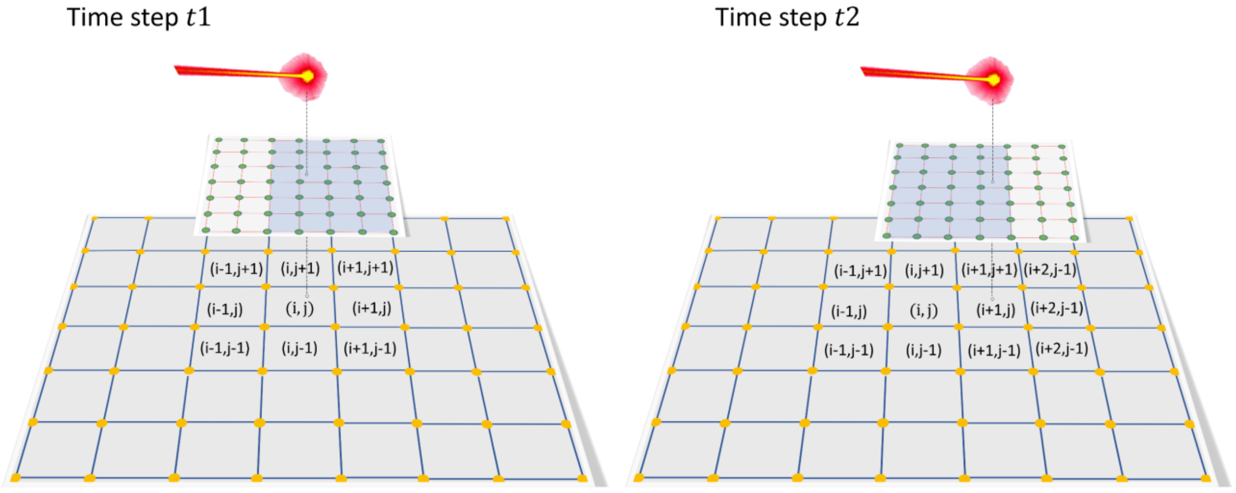

(a) (b)

Fig. 6. Demonstration of moving and remapping of fine sub-model feature of MUST-FE method using a two-levels example.

A simple two-dimensional example of a laser single-track scan induced temperature distribution is shown in Figure 8. The results of using conventional FE method with uniformly fine mesh (Figure 8a) and using a three-levels MUST-FE method (Figure 8b) shows very consistent matches, indicating good accuracy of MUST-FE solution. The Figure 9 also shows the thermal simulation result of a single track scan using a 5-level MUST-FE model. The computational time for the conventional fine uniform mesh FE solution takes ~30 minutes, while the MUST-FE method takes only 10 seconds, showing a 180 times acceleration. The high efficiency of MUST-FE method is obtained from the following factors:

- Only the high temperature gradient region is modeled with fine resolution mesh by the fine sub-model, and the rest of area is modeled with coarser resolution mesh, which reduces the total number of degree of freedoms (DOFs) in the system
- Since computation time of solving big FE sparse matrix does not scale linearly ($\mathrm{M} \cong N^2 \log(N)$), solving coarse and fine sub-domains separately partitions the model into several level smaller problems which actually save computation time to $k^{iter} m \left(\frac{N}{m}\right)^2 \log\left(\frac{N}{m}\right) \cong \frac{k^{iter}}{m} M$
- Coarse and fine mesh are pre-built, and no new node or element is introduced during the simulation. The connectivity and sparse matrix structure are also not changed during simulation which saves computation time.

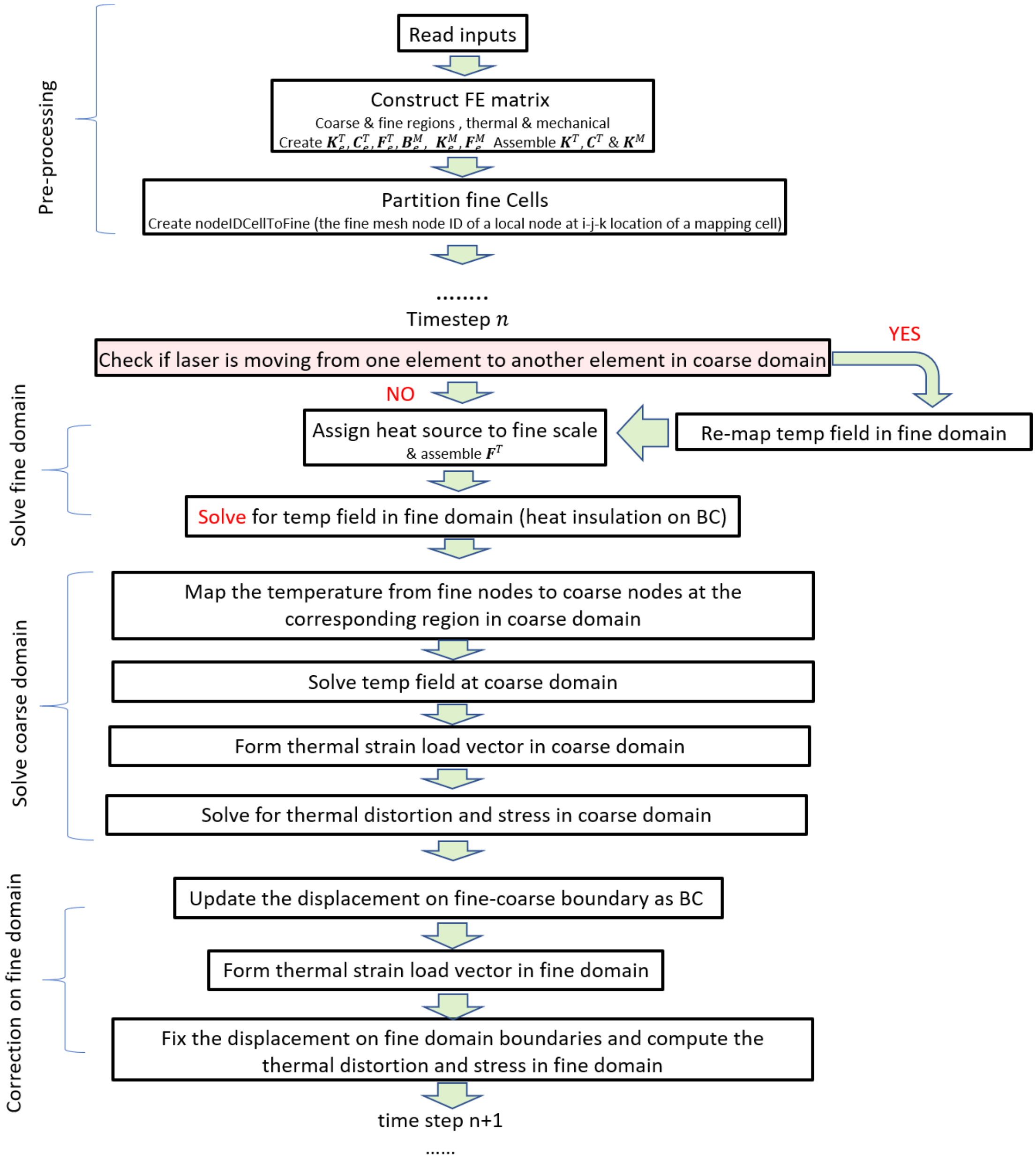

Fig. 7. Detailed algorithm of solving one time step increment

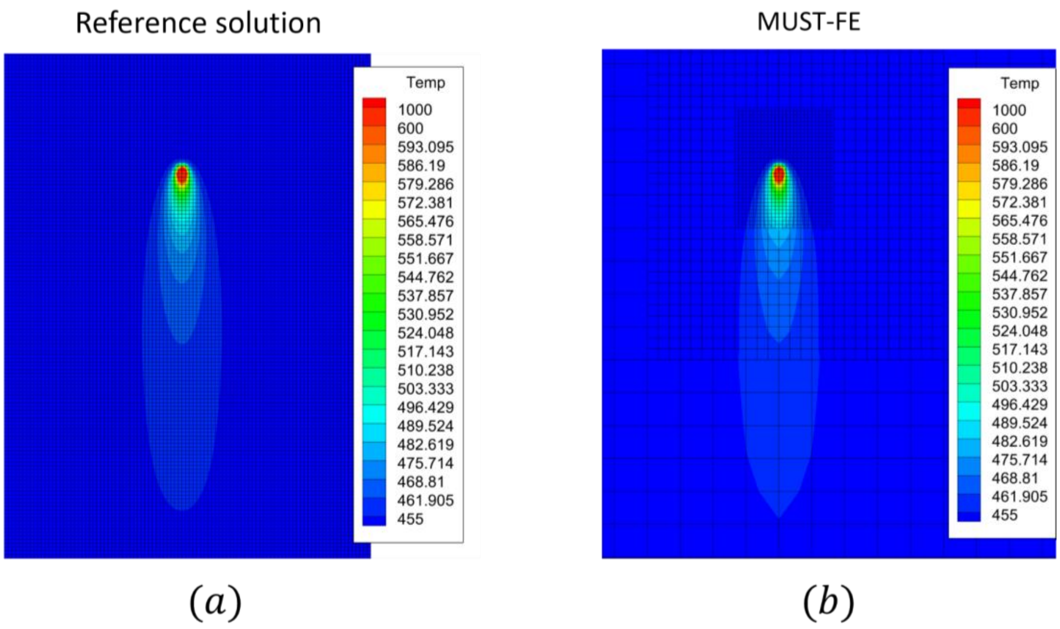

Fig. 8. Detailed algorithm of solving one time step increment

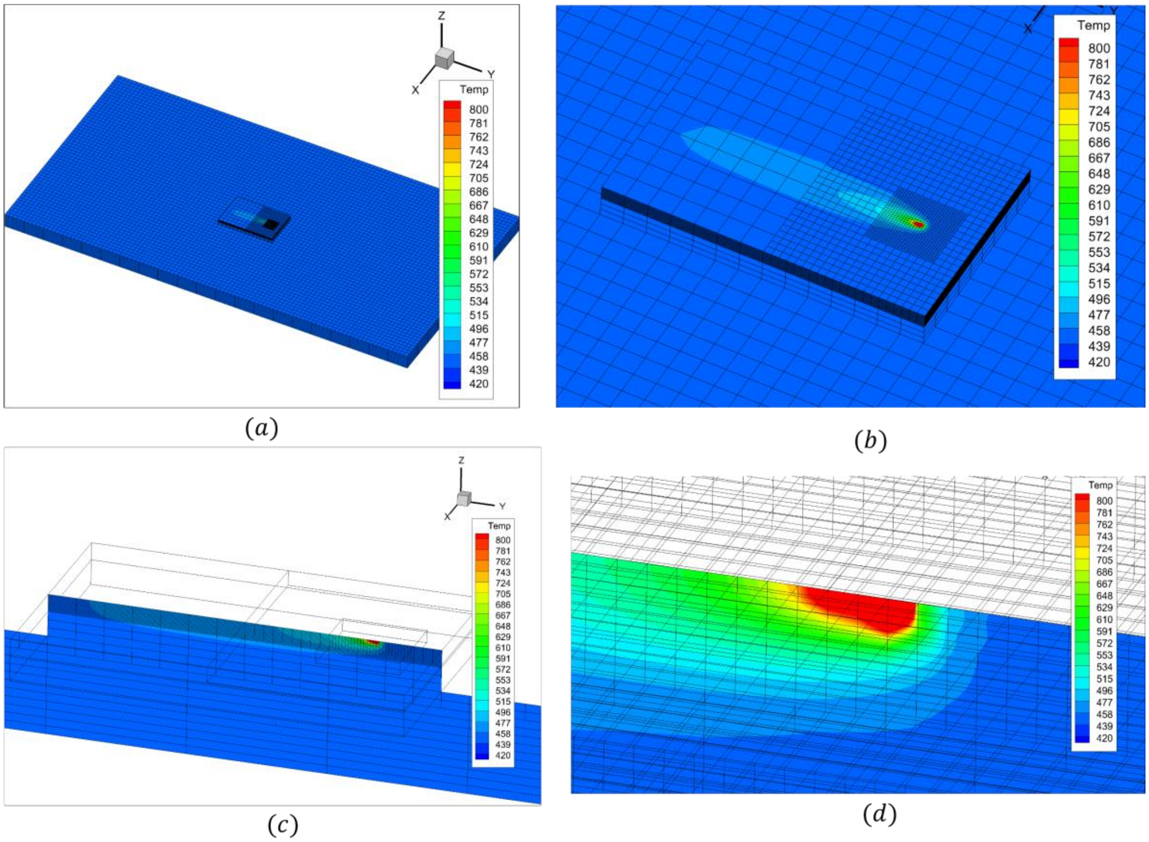

Fig. 9. Thermal simulation results of a single track using 5 levels MUST-FE. (a,b) the top view and (c,d) the cross-section view.

4.2.5Adaptive time increments at different level sub-model

An important feature of MUST-FE method is the sub-models at different level can be solved using different time step increments. Denote Δt as the time step increment in the finest sub-model, under the implicit backward Eulerian time integration algorithm, Δt is unconditionally stable and is determined by the element size of finest sub-model, i.e., $\Delta t \leq \frac{a_{\Delta t} l_f}{v}$ where v is the velocity of laser and l_f is the length of element at the finest sub-model. $a_{\Delta t}$ is a constant coefficient and is selected as $a_{\Delta t} = 0.5$. Instead of computing every coarser sub-models temperature solution every Δt increment, the level i sub-model can be computed every $n_{c:f}\Delta t$ where $n_{c:f}$ is an positive integer that satisfies $n_{c:f} \leq \frac{l_c^i}{l_f}$ and l_c^i is the length of element at the level i sub-model. That is, in Figure 7, the "solve coarse domain" and "correction on fine domain" step can be performed every $n_{c:f}$ time increments. By applying this feature, the MUST-FE computation time can be further improved up to faster compared to computing all level sub-models using the uniform finest time increments. Figure 10 shows the simulation results for a single track laser scan-induced temperature field by using different time increments at coarse sub-models. The comparison shows by using $4 \times \Delta t$ at level 1 and level 2, the simulation results is very close to the reference result (using MUST-FE with uniform Δt at all level sub-models) while the computation time is about 35% faster. By using $8 \times \Delta t$ at level 1 and level 2, the simulation results is about 60% faster, while the computed temperature field is very close to reference in the fine-model melt-pool region and have visible difference in the coarse-model far region. This result indicates the accuracy and efficiency can be adjusted by selecting appropriate $n_{c:f}$.

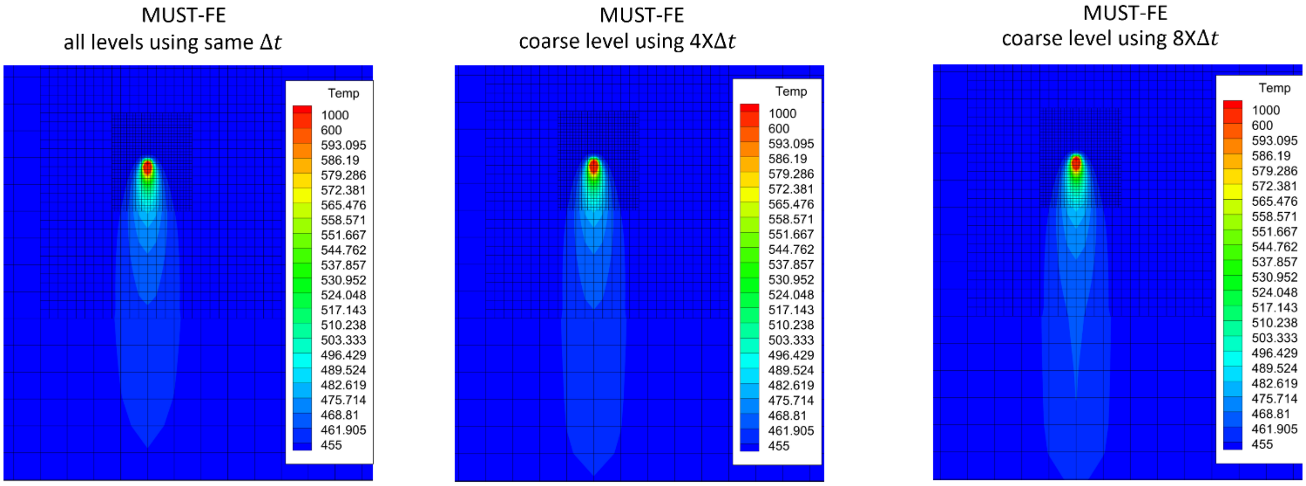

(a) (b) (c)

Fig. 10. Detailed algorithm of solving one time step increment

4.2.6 2D→3D and features for additive manufacturing

The illustrative examples of MUST-FE in section 4.2.3-4.2.5 focused on two-dimensional case studies for the easy of demonstration propose. The extension of MUST-FE method from two-dimensional to three-dimensional model requires introducing additional features for the PBF-AM. During the PBF-AM fabrication process, when the current layer has been scanned and fused, the build platform is incrementally lowered down by a small step Simultaneously, the powder chamber is raised and a coating roller then deposits another thin layer of powder across the build platform on top of the fused section. This deposition process repeats for all layers till the completion of the part. Compared to the size of the entire AM part (usually $\geq 10^{-2}m$) , the thickness of each thin powder layer (usually $\leq 10^{-4}m$) is much smaller, which requires using very fine thickness mesh in FE models. For conventional FE model, the adding of each new layer can only be achieved by adaptive element refine and coarsen in a h-fem scheme, or by using coarse thickness mesh and grouping multi-layers as one ‘effective’ layer and simplifying the simulated building process. The former method requires trivial and repeated adding and removing of nodes and elements as well as changing the sparse FE matrix structure which significantly increases the simulation time, while the later method over-simplifies the build process by reducing the number of heating-cooling cycles and reduce the accuracy by using coarse spatial resolution.

In MUST-FE framework, the adding of each new layer is achieved by taking the advantage of movable sub-domains feature (described in section 4.2.4). As illustrated in Figure 11, the entire three-dimensional LBF-AM model in MUST-FE scheme contains at least three levels. The level 1 uses coarse mesh to model the geometry of the entire part, and the mesh is fixed spatially. The level 2 sub-model accounts for adding new layers, and it uses elements that has coarse resolution in planner (transverse, or x-y) direction and fine resolution in thickness (build, or z) direction, and can move in z-direction when a new layer is added. The level 3 sub-model follows the moving of laser and captures the fine-resolution melt pool, and uses the fine resolution elements in all directions. The movement of level 3 sub-model follows the laser in x-y direction, and following the level 2 sub-model in z-direction when a new layer is deposited.

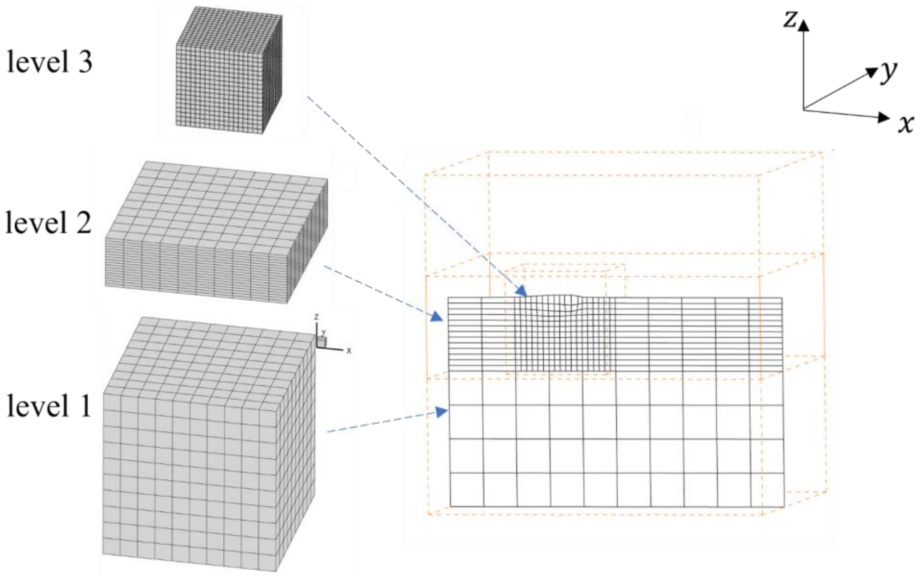

Fig. 11. Detailed algorithm of solving one time step increment

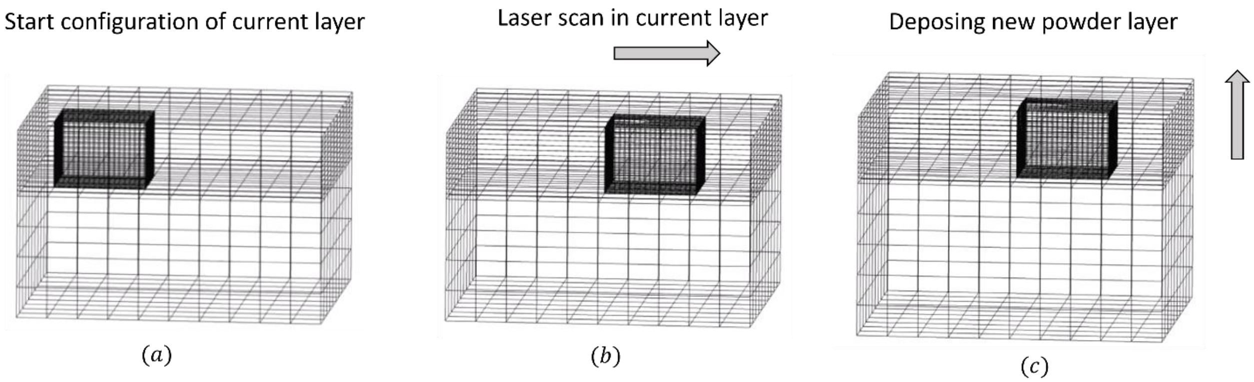

Fig. 12. Illustration of simulation process and sub-domain movement. (a) the initial configuration (b) during laser scan in a layer, the level 3 sub-model moves in planner direction following the laser, (c) when the current layer is completed and a new layer is added, the level 2 and level 3 sub-models move in z-direction to account for the new layer.

Figure 12 illustrates the MUST-FE strategy of three-dimensional three-level sub-model in a LBF-AM simulation. At the beginning of the simulation, the three-level models are created based on the following criterion:

- The coarse model contains the geometry of the entire to-be-printed part with coarse mesh
- The level 2 sub-model contains the finite thickness portion of the coarse model, i.e., it has the same geometry in planar (x-y) direction as coarse model but a finite thickness ($\geq 300\mu m$) in Z-direction. The level 2 model is meshed with very fine element thickness in Z-direction and coarse element length in X-Y direction. (see Fig. 11)
- The level 3 sub-model contains a small region around the laser and meshed in finest resolution in all directions (see Fig.11).

The three-level model performs the following movement strategy during the multi-layers LBF-AM simulation:

- During the simulation process of printing a layer i, the location of the laser is identified in the level 1 coarse model first. The elements that are above the current laser position level 1 coarse model is de-activated by removing the corresponding the degree of freedom from the to-be-solved system, and the FE vectors and matrix in equations (4-13) are therefore condensed to a smaller size. It is noted this condensation only need to be performed once at the beginning of each layer, which save simulation time.
- The level 2 sub-model is spatially fixed in X-Y direction and only move in Z-direction. Its location in Z-direction is determined by matching the top surface of the level 2 sub-model to top surface of the current activated elements of level 1 coarse model. The elements that are above the current laser position level 2 sub-model is also de-activated by removing the corresponding the degree of freedoms from the to-be-solved level 2 FE system.
- The level 3 and higher (3+) sub-models move in X-Y direction following the trajectory of the layer (which is similar to the two dimensional MUST-FE model), and the level 3+ sub-model location in Z-direction always matches level 2 sub-model, i.e., the top surface of level 3+ sub-models is aligned

to the top surface of level 2 sub-model. Similar to level 1 and level 2 sub-model, the elements that are above the current laser position level 3 sub-model is also deactivated.

Based on the above criterions, when the laser completed the printing of a current layer i and a new layer i+1 is deposited, one of the following two operation will be performed:

1. If the laser moves up to next (higher) layer elements in level 1 coarse model, then all level 2 and level 3 sub-models moves up by the same distance (i.e., the thickness of level 1 coarse element) as shown in figure 10c. All level sub-models need to re-identify the elements that are above current laser position and needs to be de-activated.
2. If the laser does not move to next (higher) layer elements in level 1 coarse model, then level 2 and level 3+ sub-models also does not move in Z-direction. However, the laser moves up in level 2 and level 3+ sub-models, and re-identification of de-activated elements need to be performed in level and level 3+ sub-models. The level 1 model does not need to re-identify the de-activated elements.

It is noted that if finer resolution is needed that level 3 sub-model, the higher level sub-models can be easily introduced to the MUST-FE system by adding finer resolution meshed smaller region located inside level 3 sub-model. The higher level sub-model will use the same allocation and moving strategy as level 3 model, i.e., move in X-Y directions following the trajectory of laser, and move in Z-direction following the level 2 sub-model.

4.2.7 Calibration and validation of the thermal part of MUST-FE model with ‘2D pad’ experiments

We calibrate and validate the developed MUST-FE model by conducting the experiments and simulation of a designed ‘two-dimensional (2D) pad’ test. The ‘2D pad’ tests were conducted by depositing AlSi10Mg tracks on “2D Pads” using SLM125 3D printer at Ford, as shown in figure 13. On each pad, 7 tests were performed, and each test was composed of conducting 7 tracks of bi-directional laser scans on one layer of AlSi10Mg powders located on the base. In each test, the laser controlling parameters for the 7-tracks were maintained as constants. The base, which has a “fish scale-like” structure (see figure 13), was also printed before the tests with AlSi10Mg powders using a machine default printing condition and the default scan strategy and rotates 67˚ every layer to minimize the potential residual stress. More than 50 tests have been conducted under various processing conditions, covering a range of laser power (250-375W in step of 25W), laser speed (1000-2200mm/s in step of 300mm/s), and 3 laser focus offsets (0.67mm, 2.67mm and 3.67mm). The powder layer thickness is 30um. The range of parameters were selected to avoid lack-of-fusion condition but covered both conduction melting mode and keyhole melting mode. The 2D pads were then cut, and the cross-section was mounted, polished, and etched, to reveal the melt pool shapes, as illustrated in figure 13.

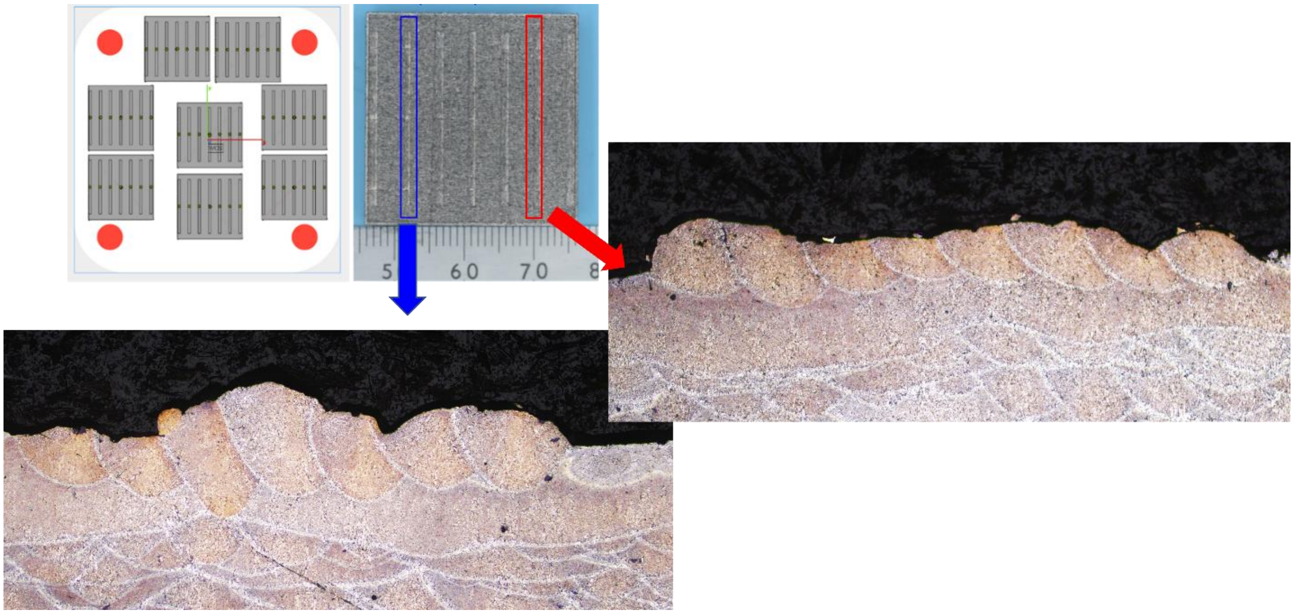

Figure 13: Demonstration of ‘2D pad’ experiments and results.

The melt pool width and depth in 2D pad tests corresponding to each set of printing parameters was measured using ImageJ Pro software. For each test, the mean melt pool depth, width and the standard deviation were calculated from the 7 tracks, and the results are listed in Table 2. The mean melt pool width and depth are plotted as a function of laser spot size in figure 14a-14c, respectively. The result revealed a clear trend that the melt pool depth increases by decreasing laser spot size, while melt pool width does not change obviously with different laser spot size. Meanwhile, the higher laser power leads to lager melt pool width and depth; and higher laser scan speed results in smaller melt pool width and depth, as expected [2]. These observations are consistent with reported trend in literatures [3]. Due to the particularities of conduction mode and keyhole mode, the melting mode is identified based on the depth-to-width (D/W) ratio of the melt pool, and a critical ratio of 0.5 is used in literature [3,4] to distinguish the two melting modes. Figure 14c shows the measured D/W ratio for each test. For a small laser spot size of $32.5\mu m$, all measured melt pool D/W ratios are greater than 0.65 which correspond to keyhole melting mode. Larger laser spot size, smaller laser power and slower scan speed decreases the melt pool D/W ratio and shift the melting mode to conduction mode, as shown in figure 14c.

Table 2. Measured ‘2D pad’ test melt pool width, depth and their standard deviation (SDV)

test ID	power (W)	speed (mm/s)	laser spot size (micron)	width (micron)	width-SDV (micron)	depth (micron)	depth-SDV (micron)
B1P2	250	1000	49.5	185.0	28.00	88.0	9.22
B2P7	250	1000	41	183.85	16.45	111.1	9.70
B2P5	250	1300	49.5	182	7.70	83	10.26
B5P7	250	1300	41	187.66	17.54	96	16.00
B4P3	250	1300	32.5	196.8	16.02	129.2	16.91
B6P3	300	1300	49.5	192.6	23.00	101.3	12.4
B2P2	300	1300	41	200.8	8.50	122.6	14.95

B4P4	300	1600	49.5	189.2	21.84	91.5	20.68
B6P4	300	1600	41	193.83	18.54	123.58	24.34
B6P1	300	1600	32.5	189.66	16.80	133.25	24.67
B2P3	325	1600	49.5	193.33	30.47	101.5	10.54
B1P6	325	1600	41	209.4	13.55	140.1	19.55
B5P6	325	1600	32.5	202.5	23.32	152.5	12.33
B5P3	375	1900	49.5	182	21.10	112.16	17.56
B4P6	375	1900	41	194.83	12.71	143	18.55
B3P6	375	1900	32.5	190.16	20.35	175.41	11.76

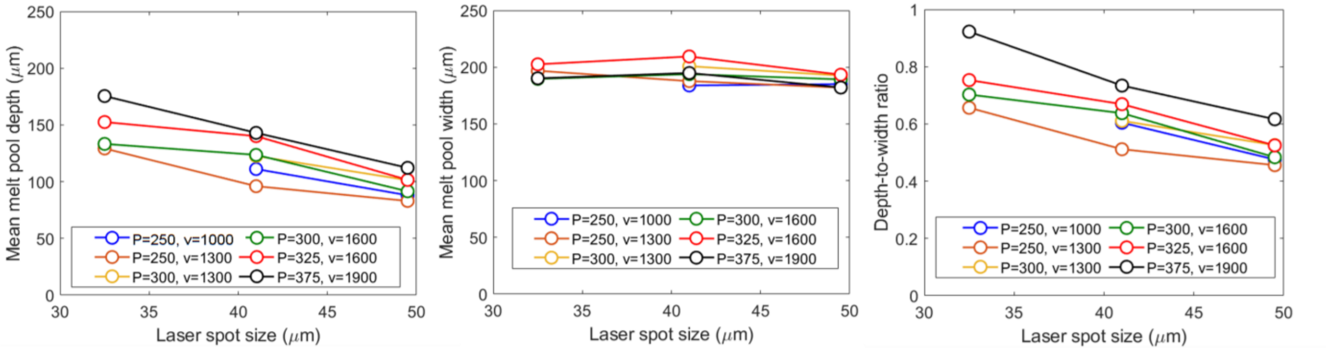

(a) (b) (c)

Figure 14: 2D pad experiment results of melt pool (a) depth (b) width and (c) depth-to-width ratio.

The MUST-FE simulations for the 2D pad experiments were conducted based on the following setup. The FE model setup is for a representative volume element (RVE) cell of $2mm \times 2mm \times 2.25mm$ region as shown in figure 15(a). The RVE contains a $30\mu m$ thick powder layer and a 2.22mm thick base. The MUST-FE model contains 4 levels sub-models. The level 1 coarse sub-model has element size of $200\mu m \times 200\mu m \times 150\mu m$, and the level 4 finest sub-model contains element size $22.2\mu m \times 22.2\mu m \times 15\mu m$. Heat convection and radiation boundary condition are applied on the top surface, and fixed temperature boundary condition is applied on the bottom surface, while the rest surfaces are assumed to be thermal insolated. The elements for the base and the powder layer are assigned to two different sets of material properties (bulk AlSi10Mg and powder AlSi10Mg), as listed in table 1. When the powder reached the solidus temperature during the laser heating, its properties will be switched to the bulk AlSi10Mg material properties, and then retain the bulk properties during the rest of the simulation.

Figure 15b illustrates the simulation predicted melt pool geometries by plotting peak-history temperature during the scanning of the seven tracks and plots the solidus temperature iso-surface, which corresponds to the surface of the melt pool boundaries. It is found the melt pool shape is strongly affected by the laser heat source model in the MUST-FE simulation. The first set of trial MUST-FE simulations were conducted based on the Gaussian semi-ellipsoid heat source model from Goldak [5], which can be expressed as:

$$Q(x,y,z)=\begin{cases}\dfrac{6\sqrt{3}f_f\eta P}{a_f bc\pi\sqrt{\pi}}\exp\left[-3\left(\dfrac{d_x^2}{a_f^2}+\dfrac{d_y^2}{b^2}+\dfrac{d_z^2}{c^2}\right)\right] & for\ d_x\geq 0\\ \dfrac{6\sqrt{3}f_f\eta P}{a_r bc\pi\sqrt{\pi}}\exp\left[-3\left(\dfrac{d_x^2}{a_r^2}+\dfrac{d_y^2}{b^2}+\dfrac{d_z^2}{c^2}\right)\right] & for\ d_x\leq 0\end{cases}\tag{16}$$

here, $Q(x,y,z)$ is the volumetric heat flux at an integration point located at coordinates (x,y,z). The laser is assumed to move along x-axis. d_x, d_y, d_z are the components of spatial distance from this integration point to the moving laser spot center located on the top surface of the model, respectively. η is the laser energy absorptivity of the material, and P is the input laser power. a_f and a_r defines the semi-axis of the semi-ellipsoid for the front ellipsoid and rear ellipsoid parts, respectively; b defines the semi-axis transverse to the laser moving direction and c defines the depth of the semi-ellipsoid, respectively. For simplicity, $a_f=a_r=b=r$ is used in this work, with r being the laser spot size (radius). The coefficients f_f and f_r are introduced to define the fraction of heat deposited in the front and rear of the heat source, where $f_f+f_r=2$. In addition, to ensure the continuity of equation (14) at d_x= 0, the constraints $\frac{f_f}{a_f}=\frac{f_r}{a_r}$ is required, and thus the values for f_f and f_r are determined. It has been reported the vapor formation in keyhole melting mode would change the absorptivity as vapor has a different rate of absorption than the molten metal [6], and therefore both absorptivity η and laser heat source depth parameter c are considered as calibratable parameters.

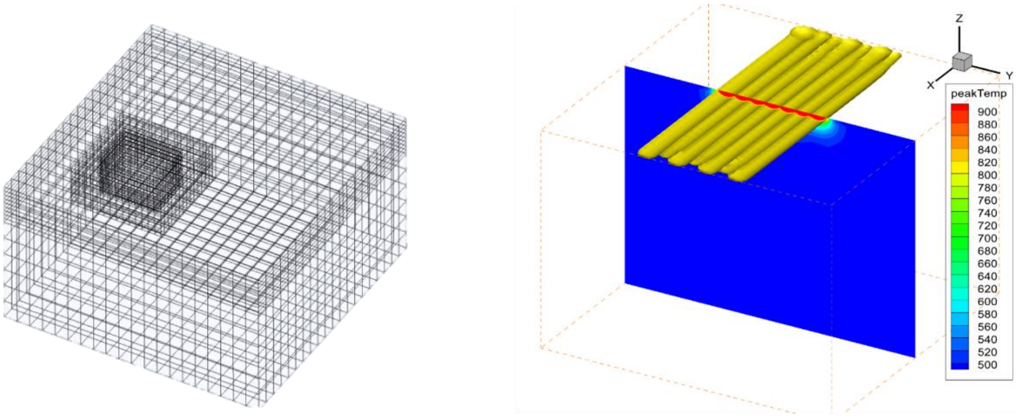

(a) (b)

Figure 15: 2D pad experiment results of melt pool (a) depth (b) width and (c) depth-to-width ratio.

However, the simulations results based on original Goldak heat source model showed the model were unable to capture the 2D pad melt pool geometries for the results in keyhole melting mode, but only in conduction melting mode. Figure 16 plotted the simulation results for laser power $P=375W$, scan speed $v=1900mm/s$ and different laser focus offset (spot size). By setting absorptivity $\eta=0.11$ and heat source depth parameter $c=30\mu m$, the simulation is able to match the melt pool width, as shown in figure 16a. However, the melt pool depth was significantly underpredicted especially at smaller laser spot size, as shown in figure 16b. Increasing heat source depth parameter c did increase the predicted melt pool depth, however, this increase is quite marginal as shown in figure 16b where an increase of c from 30μm to 90μm only led to 12μm -15μm increase of predicted melt pool depth. Increasing absorptivity η, on the other hand, has a more obvious increase in melt pool depth (see figure 16e), but it also caused significant increase and overprediction of melt pool width (see figure 16d), resulting to a nearly unchanged D/W ratio as shown in figure 16f. With all attempted absorptivity η and heat source depth parameter c, the predicted melt pool D/W ratio was always < 0.5 which corresponds to the conduction melting mode, as shown in figure 14c and 14f. These results demonstrate that just by calibrating η and c the simulation was unable to capture the keyhole melt pool formation.

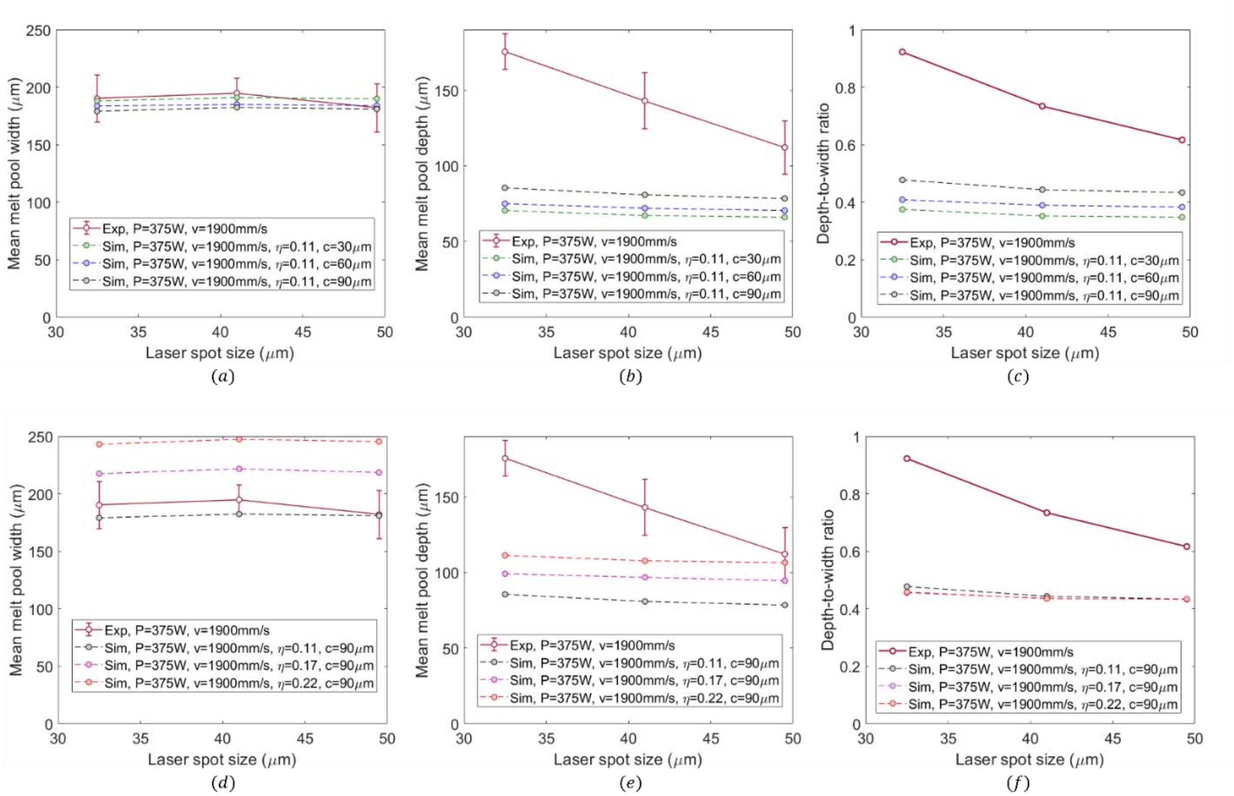

(a) (b) (c)

(d) (e) (f)

Figure 16: Comparison of melt pool (a,d) depth, (b,e) width and (c,f) depth-to-width ratio between experiment measurements and simulation results based on Goldak laser heat source model with varying values of calibratable parameters (a-c) heat source depth c and (d-f) absorptivity η.

4.2.7.1 Modified Goldak Heat Source Model

In order to model the melt pool under a broad range of process parameters using an universal heat source model, we proposed the an simple extension to the Goldak laser heat source model. The modified volumetric heat flux from laser is expressed as:

$$Q(x,y,z) = \begin{cases} \dfrac{3 f_{f/r} f_t \eta P}{a_{f/r} b d_z^0 \pi} \exp\left(-3\left(\dfrac{d_x^2}{{a_{f/r}}^2} + \dfrac{d_y^2}{b^2}\right)\right) & for \quad d_z < d_z^0 \\ \dfrac{6\sqrt{3} f_{f/r} f_b \eta P}{a_{f/r} b c \pi \sqrt{\pi}} \exp\left(-3\left(\dfrac{d_x^2}{{a_{f/r}}^2} + \dfrac{d_y^2}{b^2} + \dfrac{(|d_z| - d_z^0)^2}{c^2}\right)\right) & for \; d_z \geq d_z^0 \end{cases} \tag{17}$$

With

$$\begin{cases} f_{f/r} = f_f, \quad a_{f/r} = a_f & for\ d_x \geq 0 \\ f_{f/r} = f_r, \quad a_{f/r} = a_r & for\ d_x \leq 0 \end{cases} \tag{18}$$

The schematic of the extended heat source model is shown in figure 15b. Compare to the original Goldak model (figure 17a), a calibratable parameter d_z^0 is introduced. d_z^0 can be physically interpolated as the laser penetration depth in keyhole mode when the vapor formation occurs and the recoil pressure pushing down the underneath melt flow. Numerically, d_z^0 controls the transition from conduction mode to keyhole mode and is a function of laser power, scan velocity and laser spot size, i.e. $d_z^0 = d_z^0(P, v, r)$. When $d_z^0 = 0$, the equation (15) recovers the shape of conventional Goldak laser heat source model, and $d_z^0 > 0$ corresponds to the penetration of the laser beam into the melt pool due to the melt flow vaporization and recoil pressure. The determination of d_z^0 and absorptivity η as functions of laser power, scan velocity and laser spot size are described in section 4.1. f_t and f_b are the two additional parameters determining the partition of laser energy into the portion above and below d_z^0. The continuity of laser heat flux $Q(x, y, z)$ at d_z^0 requires $\frac{f_t}{d_z^0} = \frac{\sqrt{3} f_b}{\sqrt{\pi} c}$. In addition, the integration of equation (17) corresponds to the total absorbed power from laser, such that:

$$\int_{x=-\infty}^{x=+\infty} \int_{y=-\infty}^{y=+\infty} \int_{z=0}^{z=+\infty} Q(x, y, z) dx dy dz = (f_t + f_b)\eta P = \eta P \tag{19}$$

which requires $f_t + f_b = 1$.

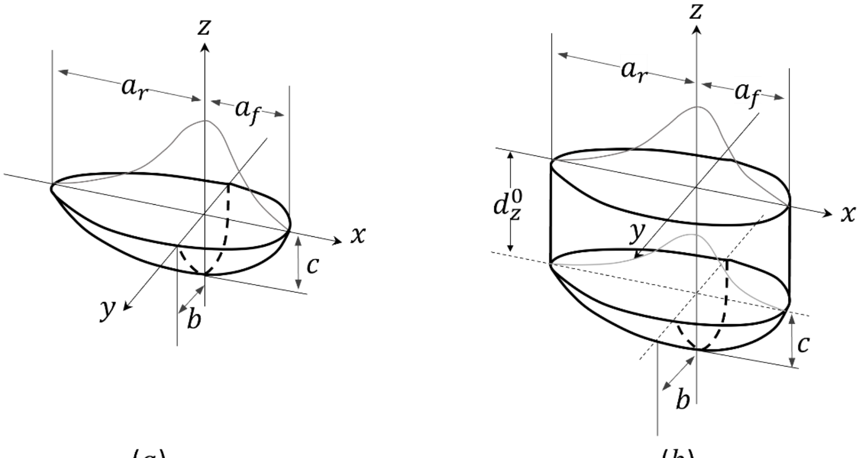

(a) (b)

Figure 17: Schematic of (a) double ellipsoidal (Goldak) heat source model, and (b) the modified Goldak heat source model

Figure 18 shows the simulation predicted melt pool geometries in two case studies. The first case corresponds to a test with input laser power of 250W, laser scan speed of 1300mm/s, laser spot size of $49.5\mu m$. The calibratable parameters were set to $\eta = 0.17$ and $d_z^0 = 0\mu m$, and the simulation predicted a conduction mode melt pool geometry, as shown in figure 16a and 16b. The second simulation corresponds to a test with input laser power of 375W, laser scan speed of 1900mm/s, laser spot size of $32.5\mu m$. The calibratable parameters were set to $\eta = 0.27$ and $d_z^0 = 160\mu m$, and the simulation predicted a keyhole mode melt pool geometry, as shown in figure 16c and 16d. In both cases, the parameter c in the laser heat source model is fixed at $c = 30\mu m$. The simulation results demonstrate that even though the proposed modification in this work is rather simple, the modified Goldak heat source model achieves good versality in the sense that by choosing appropriate absorptivity η and penetration depth d_z^0 the model is able to capture both the conduction and keyhole melting modes.

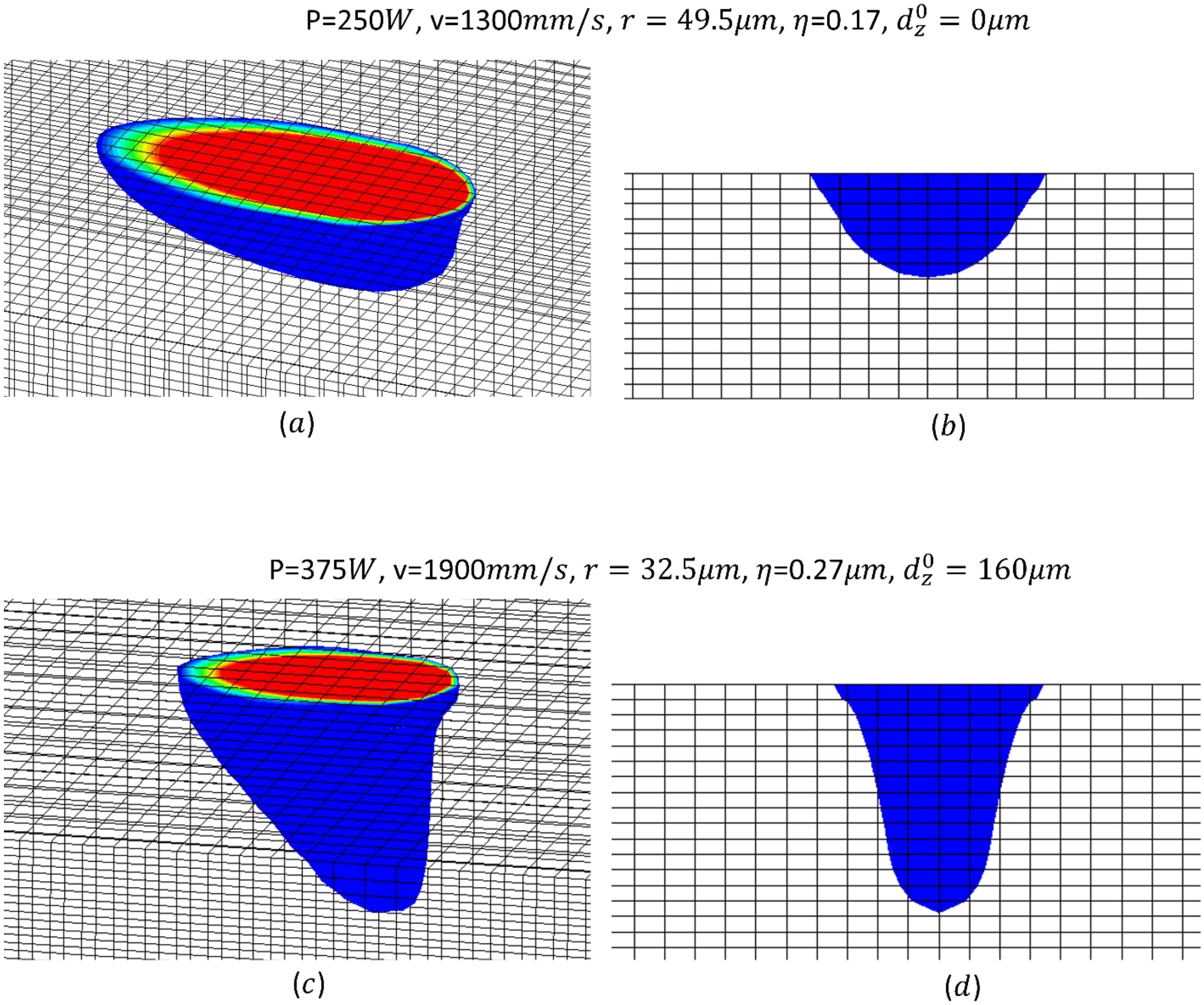
P=250W, v=1300mm/s, $r = 49.5\mu m$, η=0.17, $d_z^0 = 0\mu m$

(a) (b)

P=375W, v=1900mm/s, $r = 32.5\mu m$, η=0.27μm, $d_z^0 = 160\mu m$

(c) (d)

Figure 18 Simulation results based on the proposed extended Goldak heat source model, which captures (a) conduction model melt pool shape and (c) keyhole mode melt pool shape. The melt pool shape are drawn by removing the regions with temperature below the solidus temperature. (b) and (d) are the views along laser moving direction for (a) and (c), respectively.

4.2.7.2 Gaussian Process (GP) surrogate method to determine d_z^0 and η

At this point, in order to apply the modified Goldak heat source model to correctly model the melt geometries under varying test conditions in MUST-FE framework, it is critical to establish the relation between the calibratable parameters (absorptivity η and laser penetration depth d_z^0) and the laser process condition parameters (laser power P, scan speed v and laser spot size r), i.e., identifying the functional form $\eta = \eta(P, v, r)$ and $d_z^0 = d_z^0(p, v, r)$. This function must be estimated from the available experimental data but this task is not straight forward as iteration will be necessary and the finite element model is somewhat computationally expensive. Furthermore, the functional forms of $d_z^0(P, v, r)$ and $\eta(P, v, r)$ are not known a-priori. Hence, a statistical approach will be adopted making use a computationally efficient surrogate model and nonparametric treatment of both desired functions. To simplify notation, we will hereafter refer to $d_z^0(P, v, r)$ simply as $f(\boldsymbol{x})$ and $\eta(P, v, r)$ as $g(\boldsymbol{x})$.

Consider that *N* physical experiments have been performed and the width and depth of the melt pool have been measured at each condition e.g. $\boldsymbol{w} = \{w_i\}_{i=1}^N$ and $\boldsymbol{h} = \{h_i\}_{i=1}^N$. For each experiment there are controlled input variables $\boldsymbol{X} = \{\boldsymbol{x}_i\}_{i=1}^N$ where $\boldsymbol{x} = (P, v, r)$. Rather than estimating the desired functions, consider instead a simpler problem of simply estimating f_i and g_i at each individual experimental setting for *i=1,…,N*. The following statistical model could be utilized to describe the data generating process,

$$w_i = s_w(\boldsymbol{X}, f_i, g_i) + \epsilon_i$$
$$h_i = s_h(\boldsymbol{X}, f_i, g_i) + v_i, \tag{20}$$

where ϵ_i and v_i are experimental Gaussian noise with zero mean and unknown variances, and s_w and s_h are the finite element model melt pool width and height estimates. Note that here we assume that the finite element model is capable of exactly describing the data and we neglect incorporation of a bias function which is sometimes included in the Bayesian calibration literature [7]. Point estimates for f_i and g_i can be estimated by minimizing the L_2 loss between w_i & s_w and h_i& s_h. Alternatively, a Markov Chain Monte Carlo (MCMC) sampler could be utilized to estimate probability densities of f_i and g_i from the statistical model. However, both cases are difficult as the finite element model is nonlinear, requiring iteration, and each simulation run is computationally expensive making direct iteration intractable. Hence, an alternative approach is needed to estimate the desired quantities.

A commonly used approach is to instead utilize a computationally efficient surrogate model to replace s_w and s_h. Establishing these surrogate models requires up-front computational cost accrued from running a fixed number of simulations over a suitable design. The inputs to the finite element model are parametric which include the prescribed experimental settings ($\boldsymbol{X}$) and unknown parameters d_z^0 and η; together $\boldsymbol{z} = (\boldsymbol{X}, d_z^0, \eta)$. In this work a M=50 run maximum projection design was utilized for probing the finite element model [8]. This design criteria is desirable since it ensures good coverage, or spread, of settings over the input space and exhibits good properties for establishing surrogate models. The parametric finite element model can be emulated using a Gaussian Process surrogate model. Consider a single finite element output scalar value, over many runs the output of these computer experiments is $\boldsymbol{y} = \{y_i\}_{i=1}^M$. Under the assumption that these outputs are from a Gaussian Process the data can be jointly modeled according to the following statistical model,

$$\boldsymbol{y} \sim \mathcal{N}(\boldsymbol{0}, \sigma_y^2 \boldsymbol{R}) \tag{19}$$

where the mean is assumed to be $\boldsymbol{0}$, σ_y^2 is the variance of the process, and data in $\boldsymbol{y}$ is correlated according to the correlation matrix $\boldsymbol{R}$. Each matrix entry captures the spatial correlation between two points $R_{ij} = \exp\left(-\frac{1}{2}\sum_{k=1}^5 \theta_k^2 \left(z_{ik} - z_{jk}\right)^2\right)$ where θ_k are roughness parameters that weigh the importance of different variables e.g. perhaps the degree of spatial ‘closeness’ is different for P and V. Note that the statistical model contains no error term as the numerical simulation is deterministic; two repeated runs yield identical results (neglecting some floating point errors). Note that this model contains hyperparameters $\boldsymbol{\theta}$ and σ_y^2 which must be estimated from the data. Point estimates of these values were obtained by maximizing the likelihood function for the statistical model (or equivalently minimizing the negative log-likelihood),

$$-\log\left(L\left(\boldsymbol{\theta},\sigma_y^2\right)\right) = M\log\left(\sigma_y^2\right) + \log\left(\det(R)\right)$$

$$\sigma_y^2 = \frac{1}{m} y^T R^{-1} y \tag{20}$$

While there are ways to establish joint multiple-output Gaussian Process surrogates we simply train two surrogates for each output (width and depth). Predictions can be made using the following formula,

$$y(\boldsymbol{z}) = \boldsymbol{r}^T \boldsymbol{R}^{-1} \boldsymbol{y}, \tag{21}$$

where r is a correlation vector $\mathrm{r_i}(\mathbf{z}) = \exp\left(-\frac{1}{2}\sum_{k=1}^{5}\theta_k^2\left(z_{ik} - z_k\right)^2\right)$. Efficacy of the surrogates can be tested by computing the leave-one-out cross validation (LOOCV) using a shortcut formula which exploits the structure in the correlation matrix. Results are shown in figure 19 and the surrogate models are indeed fairly accurate at emulating the finite element response.

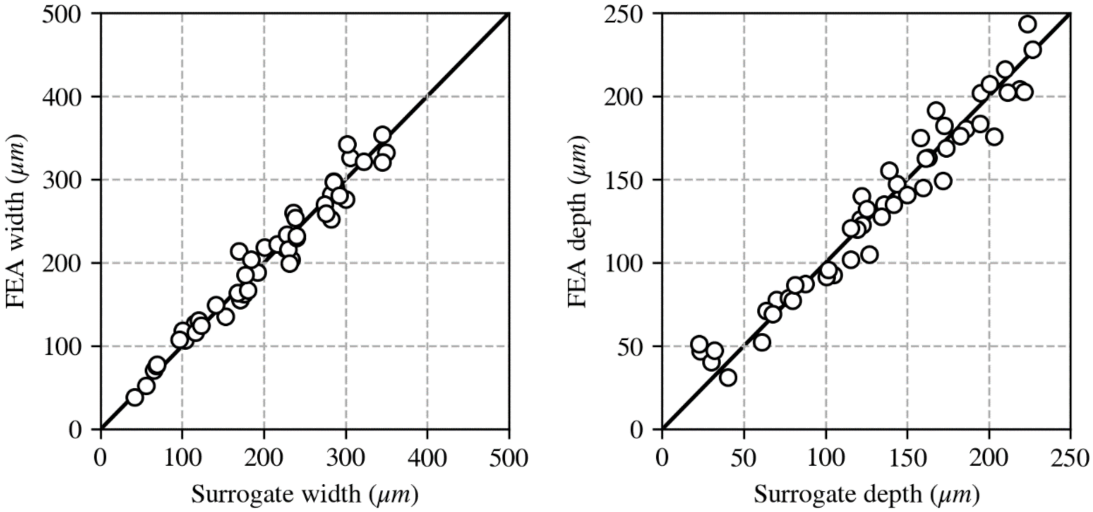

Figure 19: Leave-one-out cross validation performance of the width and depth surrogate models.

Estimates of d_z^0 and η at each experimental setting (f_i and g_i) can now easily be obtained by replacing the computationally expensive functions in Equation (20) and replacing them with the surrogate quantities. Assuming that width and depth observations are independent the likelihood function for a single experimental setting $\boldsymbol{x}_i$ can be described as,

$$p(w_i, h_i|\boldsymbol{x}_i, f_i, g_i) = \prod_{j=1}^{J} \frac{1}{\sigma_w\sqrt{2\pi}} \exp\left(-\frac{1}{2\sigma_w^2}\left(w_{ij} - \hat{s}_w\right)^2\right) \prod_{j=1}^{J} \frac{1}{\sigma_h\sqrt{2\pi}} \exp\left(-\frac{1}{2\sigma_h^2}\left(h_{ij} - \hat{s}_h\right)^2\right) \tag{22}$$

where $\hat{s}_w = \hat{s}_w(\boldsymbol{x}_i, f_i, g_i)$ and $\hat{s}_h = \hat{s}_h(\boldsymbol{x}_i, f_i, g_i)$ are the surrogate estimates of the finite element model width and height, σ_w^2 and σ_h^2 are the variances for the experimental error in observing melt pool width and height, and with the introduction of some additional notation we allow for J experimental measurements of the quantities of interest, e.g. w_{ij} is the jth repeated width measurement in experiment i. In this work we use J=5. Note, however, that the goal is to arrive at an estimate of the functions $f(\boldsymbol{x})$ and $g(\boldsymbol{x})$ and this expression only yields estimates of the discrete values f_i and g_i.

The approach adopted is taken from prior work on modeling ion-channel behavior in cardiac cells [7]. In this work the authors addressed a similar problem; given many experimental settings a functional form of a calibration parameter was desired. The key is to place a prior on the desired functions which assumes that they come from a Gaussian Process,

$$\begin{gathered} p(f) \sim \mathcal{N}\left(\mu_f(\cdot), \sigma_f^2 r(\cdot,\cdot)\right), \\ p(g) \sim \mathcal{N}\left(\mu_g(\cdot), \sigma_g^2 r(\cdot,\cdot)\right), \end{gathered} \tag{23}$$

where $\mu_f(\cdot)$ & $\mu_g(\cdot)$ are mean functions that captures global trends, σ_f^2 and σ_g^2 are the variance of the processes, and $r(\cdot,\cdot)$ a suitable spatial correlation function. In this work the mean function will be assumed to be zero which is justified by mean-centering all the data prior to analysis. The correlation function is parameterized by roughness parameters ϕ in a similar way that was previously described. Consider all these hyperparameters to be lumped together into a quantity $\boldsymbol{\Phi}$. This prior is attractive since it is completely non-parametric; no assumption of the functional form is necessary. The Gaussian Process prior essentially allows for interpolation between discrete values of f_i and g_i. However, this flexibility requires that sufficient experimental and simulated data be available to confidently infer the unknown functions. The final statistical model, which is truly the one that is desired, is

$$\begin{gathered} p(f, g|\boldsymbol{w}, \boldsymbol{h}, \boldsymbol{X}, \boldsymbol{f}, \boldsymbol{g}, \boldsymbol{\Phi}) \propto p(\boldsymbol{w}, \boldsymbol{h}|f, g, \boldsymbol{X}, \boldsymbol{f}, \boldsymbol{g}, \boldsymbol{\Phi}) p(f|\boldsymbol{w}, \boldsymbol{h}, \boldsymbol{X}, \boldsymbol{f}, \boldsymbol{g}, \boldsymbol{\Phi}) p(g|\boldsymbol{w}, \boldsymbol{h}, \boldsymbol{X}, \boldsymbol{f}, \boldsymbol{g}, \boldsymbol{\Phi}) \\ p(f, g|\boldsymbol{w}, \boldsymbol{h}, \boldsymbol{X}, \boldsymbol{f}, \boldsymbol{g}, \boldsymbol{\Phi}) \propto p(\boldsymbol{w}, \boldsymbol{h}|\boldsymbol{X}, \boldsymbol{f}, \boldsymbol{g}) p(f|\boldsymbol{f}, \boldsymbol{\Phi}) p(g|\boldsymbol{g}, \boldsymbol{\Phi}), \end{gathered} \tag{24}$$

where in the second line all the unnecessary conditionally independent terms are eliminated e.g. $\boldsymbol{w}, \boldsymbol{h}$ are only dependent on the discrete values $\boldsymbol{f} = \{f_i\}_i^N$ and not the function f itself. Likewise the functions f and g can be constructed strictly from hyperparameters $\boldsymbol{\Phi}$ and the discrete values $\boldsymbol{f}$ and do not dependent on experimentally measured width and height or the experimental process settings. The posterior distribution of the desired functions, f and g, is therefore constructed from the likelihood of the experimental data and priors placed on f and g. $p(f|\boldsymbol{f}, \boldsymbol{\Phi})$ and $p(g|\boldsymbol{g}, \boldsymbol{\Phi})$ can be easily computed from multivariate normal formulae. The unknown parameters associated with this model are: σ_w and σ_h, the experimental observation variances, N discrete values in f and g, and hyperparameters $\boldsymbol{\Phi}$. We obtained a discrete sample from these variables using Python MCMC sampler emcee [9]. No priors (uniform priors) were placed on f and g. Note that additional priors can be placed on any of the hyperparameters and we found it useful to place fairly tight priors on $\phi \sim \mathcal{N}(1, 0.1^2)$. The choice of priors on roughness parameters is known to affect solution accuracy [10]. In earlier referenced work on cardiac cell modeling the roughness parameter is fixed based on some physical knowledge of the system [7].

In addition, we employ one final data pre-processing step. In order to perform efficient experiments only a subset of the (P, v, r) space was considered; a near two-dimensional plane with near constant energy density e.g. $\frac{P}{v} = const$. This can be seen in Figure 1. We found that treatment of the problem in the original (P, v, r) space was problematic. We suspect that this has to do with the functional form of the correlation function $corr(\boldsymbol{x}_i, \boldsymbol{x}_j) = \exp\left(-\frac{1}{2}\sum_{k=1}^{3} \phi_k^2 (x_{ik} - x_{jk})^2\right)$ e.g. each component of x contributes independently. However, in the experiments P and v are in concordance. Hence, we performed principal component analysis (PCA) to obtain a transformation from (P, v, r)-space to a new coordinate system prior to performing the analysis. This can be done by a simple matrix multiplication $\boldsymbol{x}' = \boldsymbol{W}\boldsymbol{x}$ where $\boldsymbol{W}$ is obtained from PCA theory. This will also be useful later on for predicting functions f and g since predictions should be restricted to near the plane defined by $\frac{P}{v} = const$ which is captured by the new PCA mapping $\boldsymbol{W}$.

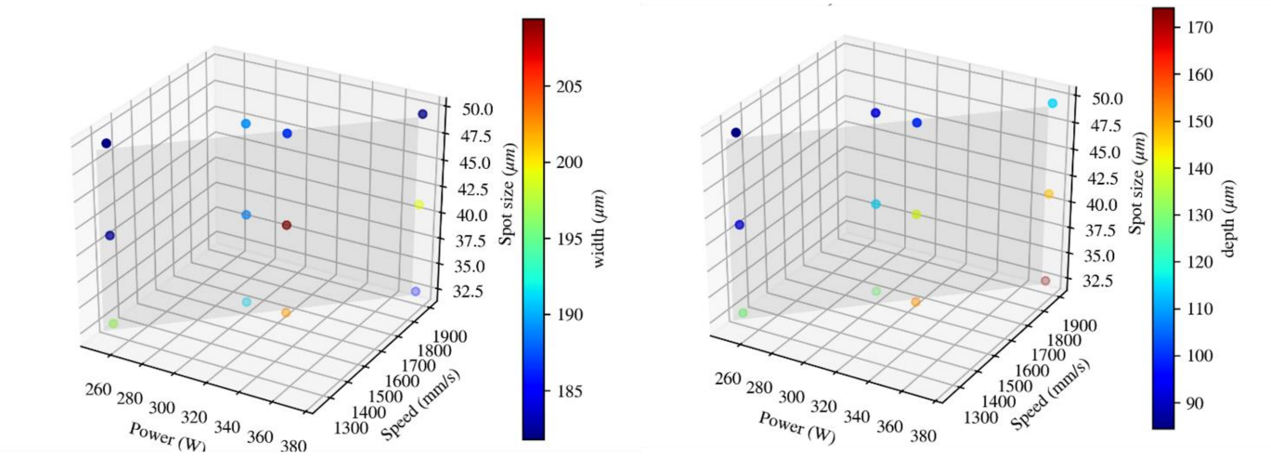

(a) (b)

Figure 20. Experimentally observed melt pool width and depth over 12 experimental settings. Approximate two-dimensional plane near which experiments we performed is shown.

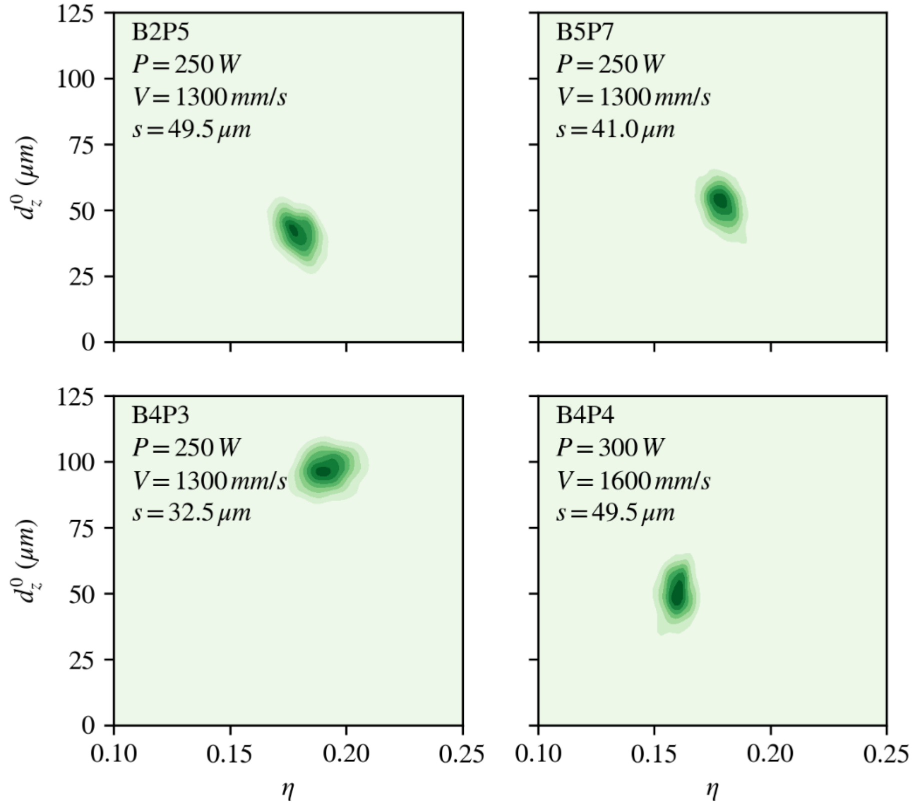

Figure 21. Estimated densities for d_z^0 and η from the MCMC sampling for a few select experiments.

4.2.7.3. Identify η and d_z^0 for each 2D pad experiment test

Using the trained GP surrogate model for η and d_z^0, the probability densities for η and d_z^0 corresponding to differing experimental settings were identified and illustrated for four marginal varying experiments as shown in figure 21. Three of these experiments share identical power and speed and only vary the laser spot size. With decreasing spot size it can be seen that the absorptivity increases and the parameter d_z^0 increases. In other words, as the spot energy becomes more focused, there is a tendency for the heat source to be driven further beneath the surface, which, increases energy transfer from the laser source.

Figure 22 illustrates the disparity between the mean measured weld pool width and depth and predictions from the surrogate. Dispersion in the histogram is from uncertainty in the estimated parameters η and d_z^0 as well as uncertainty in other hyperparameters needed in the statistical model from Equation (24). In general the fit is good; predictions are generally within +/-10μm with both depth and width predictions being generally symmetric and centered around 0.

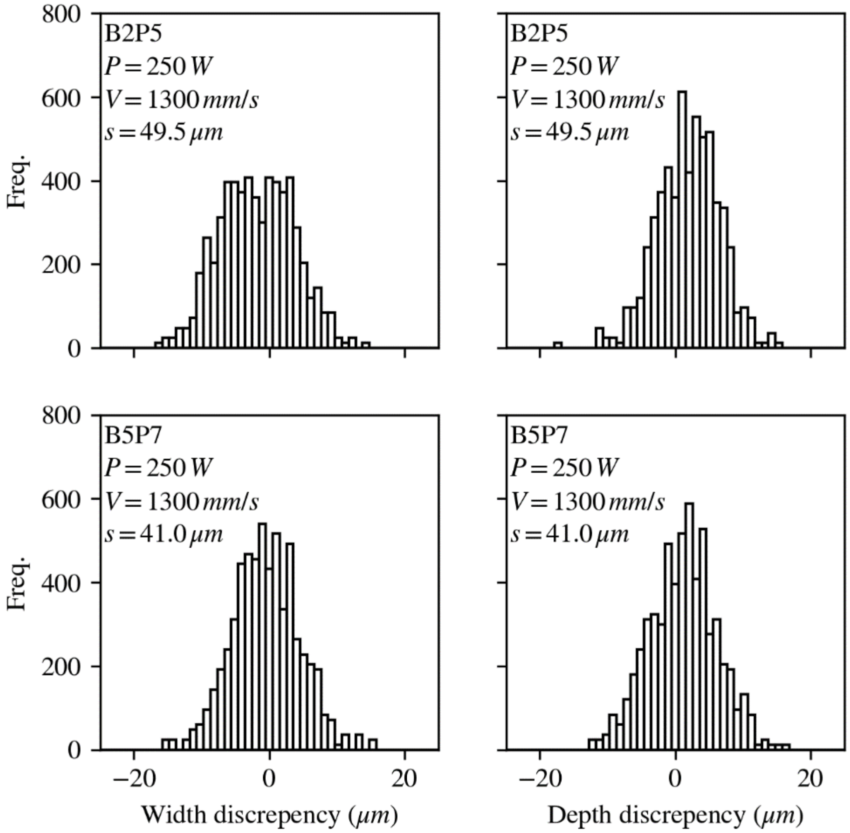

Figure 22. Discrepancy between mean experimental width and depth and MCMC predicted width and depth for a few select experiments.

Finally, predicted mean values obtained from MCMC sampling of the posterior distribution for η and d_z^0 are shown in Figure 23. In addition, a prediction of the functional quantities along a plane along $\frac{P}{v} = const$ is shown. The trend for d_z^0 agrees with physical intuition; with increasing speed/powder, or decreasing spot size, there is an increasing tendency for keyholing to occur. The absorptivity behavior follows a similar trend; with decreasing spot size and decreasing speed or powder the absorptivity increases. The values of η and d_z^0 for each of the 12 2D pad experiment tests are listed in table 3.

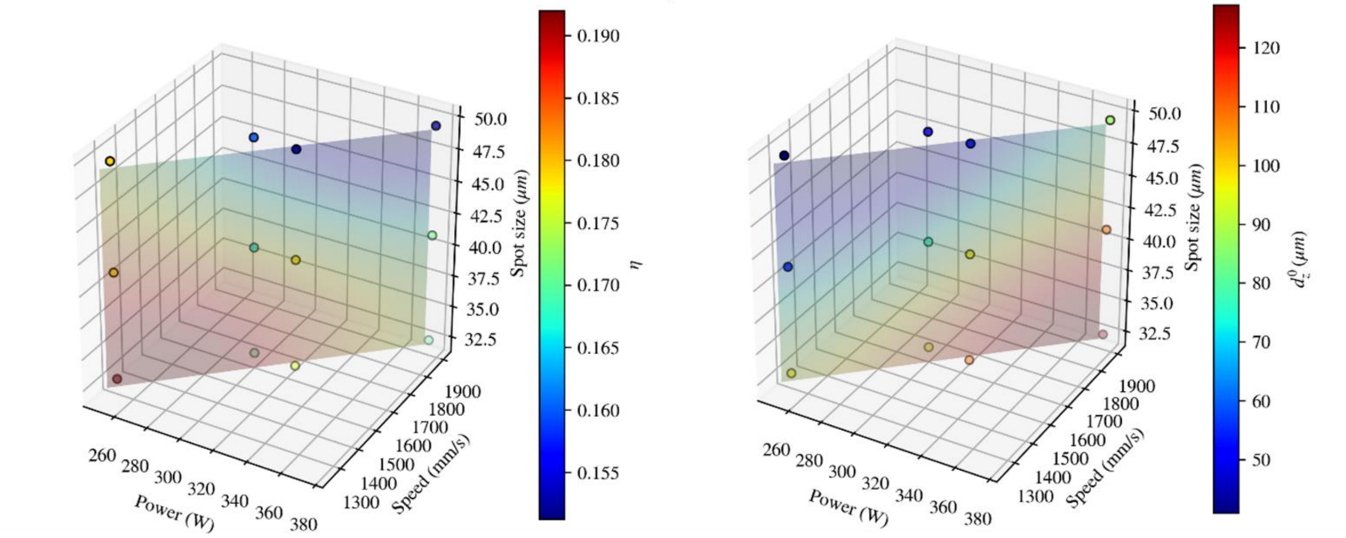

(a) (b)

Figure 23. Estimated mean functional values for (a) d_z^0 and (b) η over the experimental plane considered.

Table 3. Parameters η and d_z^0 for each 2D pad test determined using trained GP surrogate model

Power(W)	speed (mm/s)	laser spot size (μm)	Absorptivity η	penetration depth d_z^0 (μm)
250	1300	32.5	0.154	35
250	1300	41	0.185	45.2
250	1300	49.5	0.262	85
300	1600	32.5	0.165	39
300	1600	41	0.225	77
300	1600	49.5	0.235	90
325	1600	32.5	0.16	55
325	1600	41	0.22	101
325	1600	49.5	0.235	113
375	1900	32.5	0.172	83
375	1900	41	0.215	105
375	1900	49.5	0.235	135

4.2.7.4. 2D Pad simulation results using the modified Goldak laser heat source model

Finally, the 2D pad simulations were conducted based on the modified Goldak laser heat source model and the parameters identified from GP surrogate model-based calibration process. The simulation predicted melt pool depth, width and D/W ratio for all 12 2D pad tests are compared to the corresponding experiment measurements in figure 24a-24c, respectively. In general, satisfactory matching are obtained for most of the cases, except a slight overprediction of the melt pool depth in the case of P=375W, $v = 1900 mm/s$ and $r = 49.5 \mu m$, and a slight overprediction of melt pool width in the case of P=300W, $v = 1600 mm/s$ and $r = 32.5 \mu m$. The cross-sections of the seven tracks melt pool are also drawn in figure 25 in two cases, for visualization of the simulation predicted melt pool geometries under conduction mode and keyhole mode. As discussed in section 3, the matching between the simulation results and experiments was not feasible using the original Goldak heat source model, showing the robustness of this new proposed method.

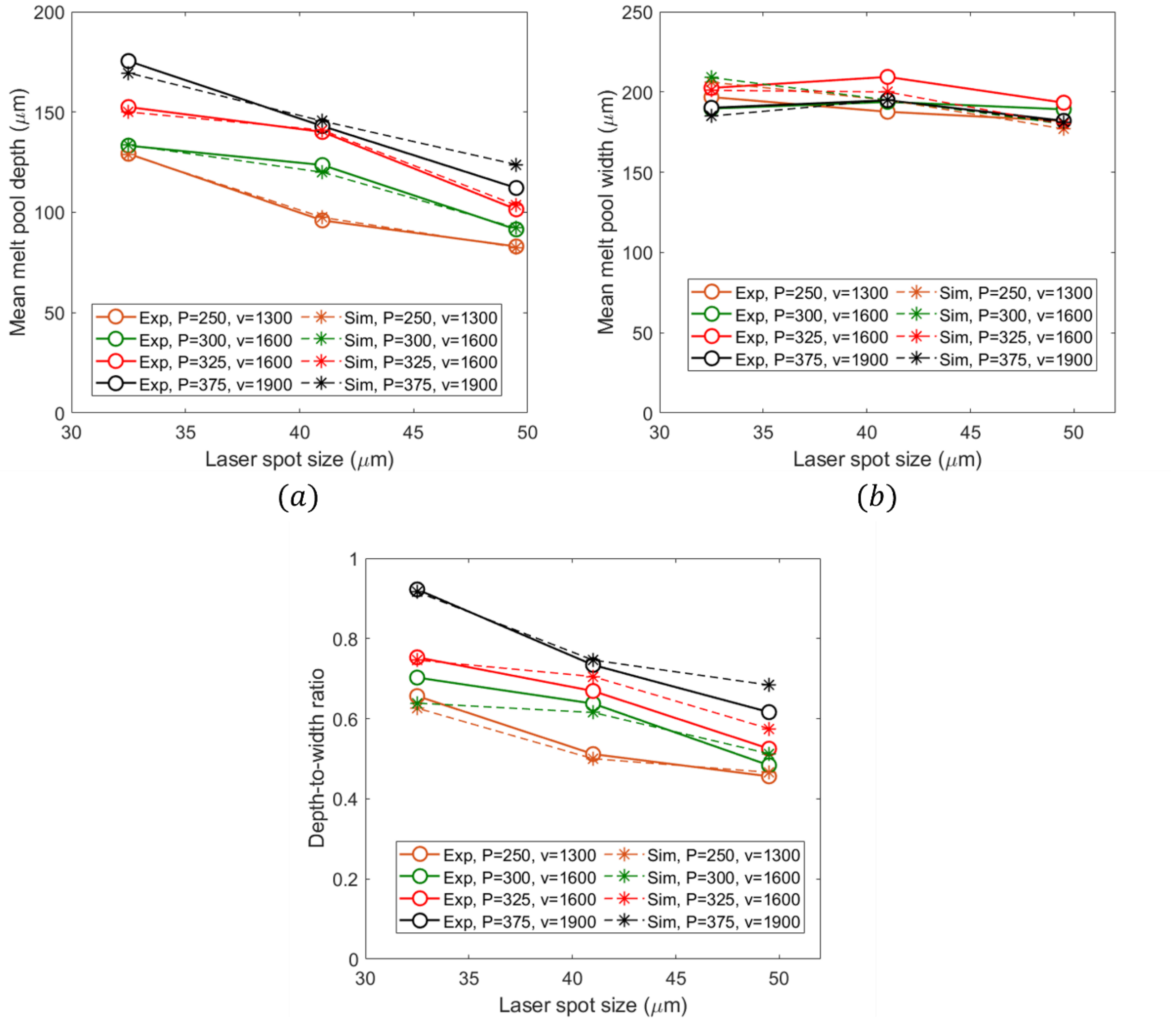

(a) (b)

(c)

Figure 24. comparison of the simulation predicted and measured melt pool (a) depth (b) width, and (c) D/W ratio for each 2D pad tests.

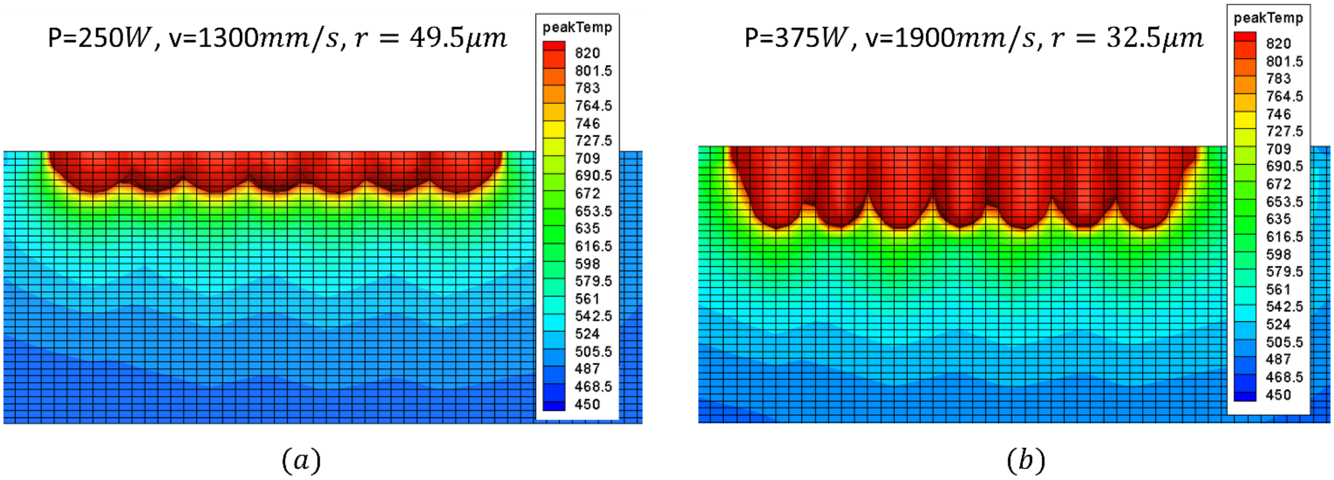

Figure 25. Visualization of the simulation predicted melt pool geometries under (a) conduction mode and (b) keyhole mode

4.2.8 Computing mechanical deformation and residual stress using MUST-FE method

The mechanical deformation and stress are computed in MUST-FE framework based on the infinitesimal strain assumption. In an incremental solution process delineated by an interval between time t and t + △t, the weak form of the equilibrium equation can be obtained from the principle of virtual work and is expressed as:

$$\int_{\Omega} \delta\boldsymbol{\varepsilon}: \boldsymbol{\sigma}^{t+\Delta t} d\Omega = \oint_{\Gamma} \delta\boldsymbol{u} \cdot \boldsymbol{t}^{t+\Delta t} d\Gamma + \int_{\Omega} \delta\boldsymbol{u} \cdot \boldsymbol{b}^{t+\Delta t} d\Omega \tag{25}$$

where $\boldsymbol{u}$ is the to-be-solved displacement, and $\delta\boldsymbol{u}$ is the virtual displacement following variational calculus theory such that $\delta\boldsymbol{u} = \{\delta u_i \boldsymbol{e}_i \in H^1(\Omega), \delta\boldsymbol{u} = \boldsymbol{0} \ on \ \Gamma\}$. $\boldsymbol{\varepsilon} = sym(\boldsymbol{\nabla u})$ is the strain tensor, and $\delta\boldsymbol{\varepsilon} = sym(\boldsymbol{\nabla}\delta\boldsymbol{u})$ is the virtual strain. $\boldsymbol{t}^{t+\Delta t}$ is the external traction force applied on surface region Γ, and $\boldsymbol{b}^{t+\Delta t}$ is the applied body force on the model volume Ω. The entire right-hand side of equation (25) is the external virtual work and will be denoted as δW^{ext}. The increment of stress, i.e. $\Delta\boldsymbol{\sigma} = \boldsymbol{\sigma}^{t+\Delta t} - \boldsymbol{\sigma}^{t} = \dot{\boldsymbol{\sigma}}\Delta t$, is computed from the following rate-independent J2 plasticity model with power-law hardening:

Small strain decomposition:

$$\boldsymbol{\varepsilon} = \boldsymbol{\varepsilon}^{\mathrm{e}} + \boldsymbol{\varepsilon}^{\mathrm{p}} + \boldsymbol{\varepsilon}^{T} \tag{26}$$

Stress-strain constitutive equation:

$$\dot{\boldsymbol{\sigma}} = \mathbb{C}^{e}: \dot{\boldsymbol{\varepsilon}}^{\mathrm{e}} \tag{27}$$

Associated flow rule:

$$\dot{\boldsymbol{\varepsilon}}^{\mathrm{p}} = \dot{\lambda}\frac{\partial f}{\partial \boldsymbol{\sigma}} = \frac{3}{2}\dot{\varepsilon}_p \frac{\boldsymbol{\sigma}'}{\sigma_e} \tag{28}$$

Yield surface equation:

$$f = \sigma_e - \sigma_f \tag{29}$$

Power-law hardening law:

$$\sigma_f = \sigma_y \left(1 + \frac{E\varepsilon_p}{\sigma_y}\right)^N \tag{30}$$

Thermal expansion:

$$\boldsymbol{\varepsilon}^{\boldsymbol{T}} = \boldsymbol{\alpha} T \tag{31}$$

Where $\dot{\boldsymbol{\varepsilon}}^{\mathrm{e}}$, $\dot{\boldsymbol{\varepsilon}}^{\mathrm{p}}$, and $\dot{\boldsymbol{\varepsilon}}^{\mathrm{T}}$are the rate of elastic strain, plastic strain and thermal strain, respectively. $\mathbb{C}^{e}$is the elastic stiffness matrix, λ is the consistency parameter, f is the yield surface function, ε_p is the effective plastic strain, $\boldsymbol{\sigma}'$ is the von Mises stress, $\sigma_e$is the effective stress, σ_f is the flow stress, and σ_y is a constant for reference yield stress. E is the Young's modulus, and N is a constant hardening parameter. $\boldsymbol{\alpha}$ is a matrix for thermal expansion which is assumed isotropic in this work. By applying equation (26-31) to equation (25) and utilizing convergence theory and mathematical derivation, the weak form for solving the mechanical displacement field can be obtained as

$$\int_{\Omega} \delta\boldsymbol{\varepsilon}: \mathbb{C}^{ep}: \Delta\boldsymbol{\varepsilon} d\Omega = \delta W_{ext}^{t+\Delta t} - \int_{\Omega} \delta\boldsymbol{\varepsilon} : \boldsymbol{\sigma}^{t} d\Omega + \int_{\Omega} \delta\boldsymbol{\varepsilon}: \mathbb{C}^{e}: \boldsymbol{\alpha} T d\Omega \tag{32}$$

Invoke the finite element discretization equations:

$$\delta\boldsymbol{u} = \boldsymbol{N}\delta\boldsymbol{q}, \qquad \delta\boldsymbol{\varepsilon} = sym\left(\frac{\partial\delta\boldsymbol{u}}{\partial\boldsymbol{x}}\right) = sym\left(\frac{\partial\boldsymbol{N}}{\partial\boldsymbol{x}}\right)\delta\boldsymbol{q} = \boldsymbol{B}\delta\boldsymbol{q}, \quad \Delta\boldsymbol{\varepsilon} = \boldsymbol{B}\Delta\boldsymbol{q} \tag{33}$$

where $\boldsymbol{q}$ is the nodal displacement vector and $\mathbb{C}^{ep}$ is the elastic-plastic tangent stiffness matrix. The to-be-solved the mechanical field weak form equation in FE matrix form is expressed as:

$$\boldsymbol{K}^{mech}\Delta\boldsymbol{q} = \boldsymbol{f}^{ext} - \boldsymbol{f}^{int} + \boldsymbol{f}^{T} \tag{34}$$

where

$$\boldsymbol{K}^{mech} = \sum_{\boldsymbol{e}}^{N_{elem}} \int_{\Omega_{\mathrm{e}}} \boldsymbol{B}^{T}: \mathbb{C}^{ep}: \boldsymbol{B} d\Omega_{e} \tag{35}$$

$$\boldsymbol{f}^{ext} = \sum_{\boldsymbol{e}}^{N_{elem}} \oint_{\Gamma_{\mathrm{e}}} \boldsymbol{N}^{T}\boldsymbol{t}^{t+\Delta t} d\Gamma_{\mathrm{e}} + \sum_{\boldsymbol{e}}^{N_{elem}} \int_{\Omega_{\mathrm{e}}} \boldsymbol{N}^{T}\, \boldsymbol{b}^{t+\Delta t} d\Omega_{\mathrm{e}} \tag{36}$$

$$\boldsymbol{f}^{int} = \sum_{\boldsymbol{e}}^{N_{elem}} \int_{\Omega_{\mathrm{e}}} \boldsymbol{B}^{T}\boldsymbol{\sigma}^{t}\, d\Omega_{\mathrm{e}} \tag{37}$$

$$\boldsymbol{f}^{T} = \sum_{\boldsymbol{e}}^{N_{elem}} \int_{\Omega_{\mathrm{e}}} \boldsymbol{B}^{T}\mathbb{C}^{e}\boldsymbol{\alpha} T\, d\Omega_{\mathrm{e}}$$

where ΔT is the temperature increment in each element computed from the thermal part of MUST-FE model. Due to the plastic deformation and non-linear hardening law, the mechanical part of MUST-FE models is non-linear system and the equation (34) is solved in an Newton-iterative algorithm via updating $\boldsymbol{K}^{mech}$ and $\boldsymbol{f}^{int}$. The nodal displacement increment $\Delta\boldsymbol{q}$**,** the stress and plastic strain fields at the integration points are solved as outputs. It is noted that the mechanical fields are solved on each level sub-model separately using the temperature increments in each sub-model. The computing algorithm requires solving the coarsest level first and then interpolating the displacement of interface nodes to the finer level sub-model (see Figure 4) as boundary conditions, which enforces the continuity of displacement across the boundaries between two conjugate level sub-models. The stress field and plastic strain fields, however, are not continuous in this method. Figure 24b shows the hydrostatic stress field (unit: MPa) computed from a single-track laser scan corresponding to the resulting temperature field in Figure 24a. The cross-section across the center of laser path is shown in Figure 25a-25c for temperature field, stress field and equivalent plastic strain field, respectively.

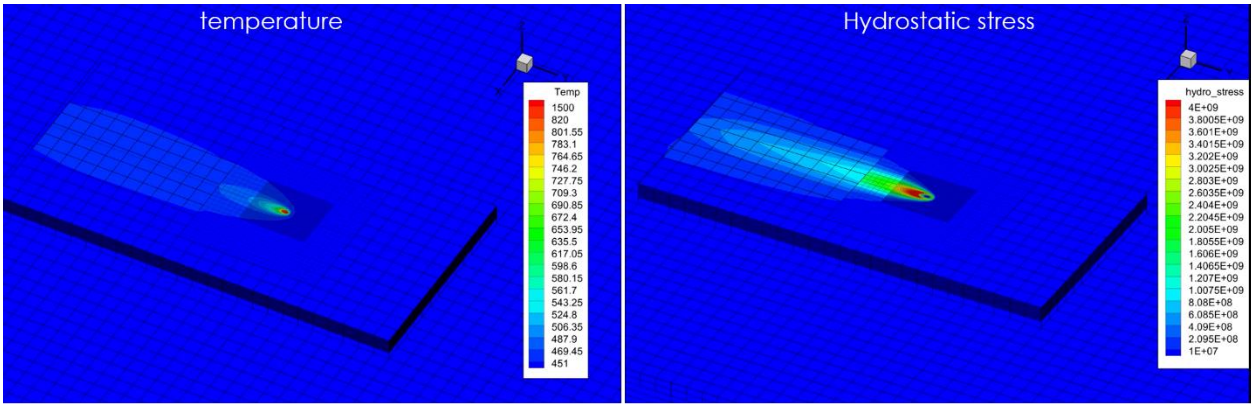

(a) (b)

Figure 26. (a) temperature (unit: K) and (b) hydrostatic stress field (unit: MPa) computed from a laser-PBF-AM single-track laser scan process.

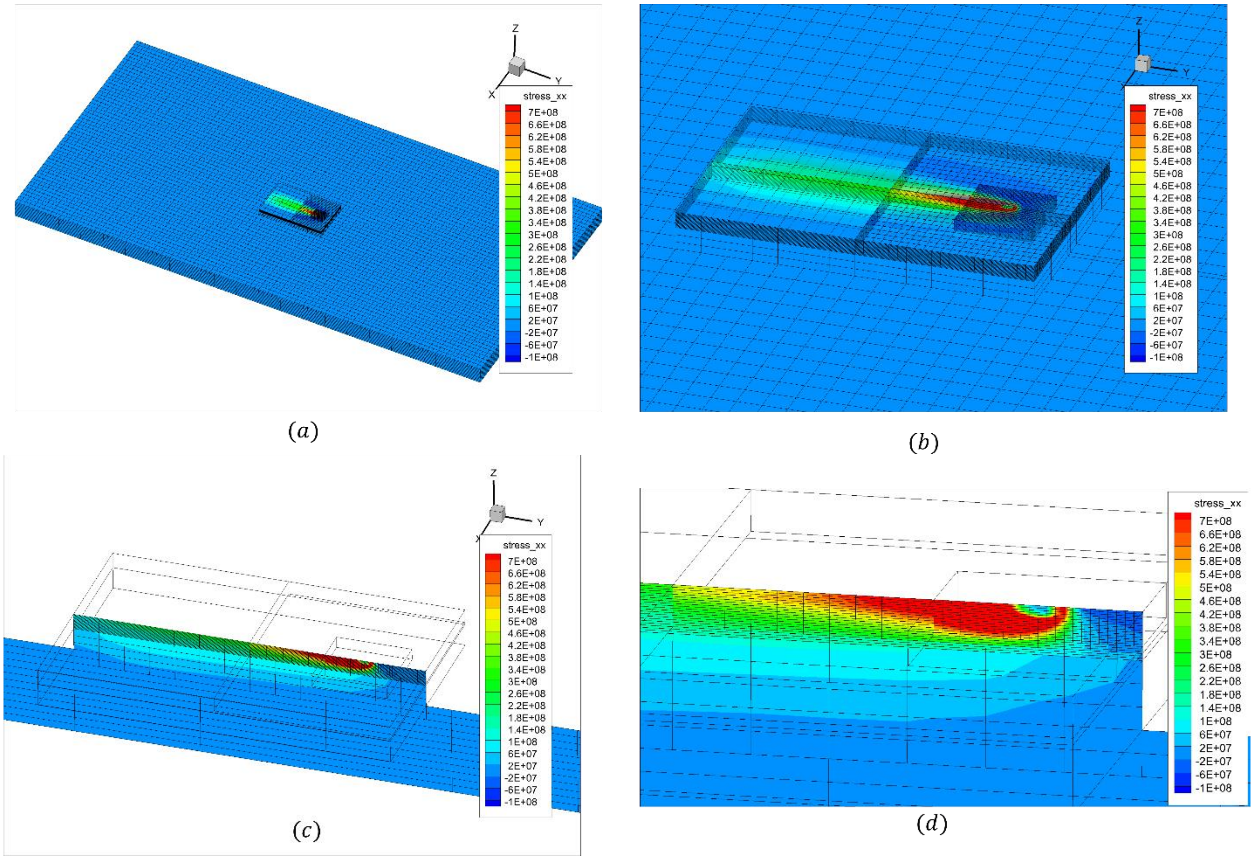

(a) (b) (c) (d)

Figure 27. The cross-section view of (a) temperature (unit: K) and (b) hydrostatic stress field (unit: MPa) and (c) plastic strain field computed from a laser PBF-AM single-track laser scan process.

4.3 Conduct Simulations for X-Y Asymmetry Demo-samples on HPC using the 3D MUST-FE code

The multi-spatial-temporal resolution concurrent FE code has been applied to simulate the laser-powder bed fusion printing process of a AlSi10Mg “XY sample” at Ford for demonstration and validation. The printed sample is around 105mm long, 55mm wide and 4mm thick, as shown in figure 28. The MUST-FE simulation model is constructed using 5-levels hierarchy, including coarse substrate (level 0, 2772 elements), fine substrate and printing part (level 1, 23770 elements), finer top region of printing part (level 2, 24440 elements), and two further refined regions that moves with the laser (level 3 and 4, 8820 and 14580 elements, respectively), as shown in figure 29. The level 0 coarse substrate is constructed using element size of 5mm*5mm*1mm, while the finest level 4 uses element of 110μm*110μm*30μm to resolve the fine temperature gradients and melt pool for laser. The part is composed of 67 or 133 layers (each layer can have a thickness of 30μm or 30 μm), and each layer contains about 400-1500 tracks (depends on the scanning parameters, which is described in section 4.5).

The model boundary condition is applied by assigning radiation and convection on the top surfaces during printing each layer, and fixing the displacement of the bottom (Z-) surface and four transverse surfaces ($\pm$X, $\pm$Y). The laser parameters are the same as used in section 4.2.7. The mechanical properties of the AlSi10Mg part, including the elastic modulus, Poisson’s ration, thermal expansion coefficient are assigned as functions of (1) solid or powder phase, and (2) the local temperature, which are adopted from [1]. In addition, a yield stress σ_y 100MPa and hardening parameter ($N = 0.4$) is used for the plasticity model. The chamber is pre-heated to a temperature of 150^oC, which is set as the initial temperature and substrate/environment temperature in the model. After printing all layers, the model is cooled down to room temperature (20^oC). In addition, after finishing printing each layer, a new layer of AlSi10Mg powder is loaded into the chamber, which is modeled by activating a new layer of fine elements in the MUST-FE framework. This loading process takes about 10 seconds and is long enough for the printed part to cool to the substrate and environment temperature. The cooling during powder loading and final colling stages are both modeled in the MUST-FE framework using a self-adaptive time increment method, which gradually increase the time increments for the thermal dispersion (since there is no laser heat source) to accelerate the simulation.

Figure 30 illustrates how the model resolve the temperature field and melt pool during the printing process, which captures the heat flux from the moving laser to the printed part and the substrate and the fine resolution melt pool. The deformation (strain) and stress field induced by thermal gradient during printing process is also computed and as shown in Figure 31a and 31b, respectively. The MUST-FE model run on ORNL CADES system using 12 processors, and simulating the printing process of each layer takes ~2hr 15mins, which is at least 1 orders faster than conventional mesh-refinement based FE method for simulating such a large part with the same resolution. The model is used to simulate the entire printing process of all 133 layers, which takes ~ 18200 minutes (12.5 days).

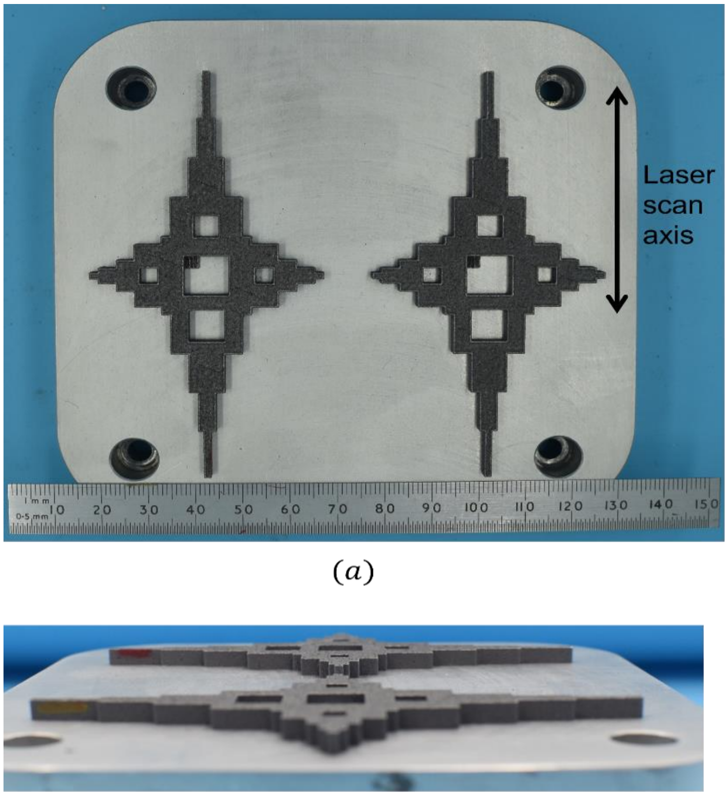

(a)

(b)

Figure 28. Printed AlSi10Mg X-Y cross samples (a) top view (b) side view

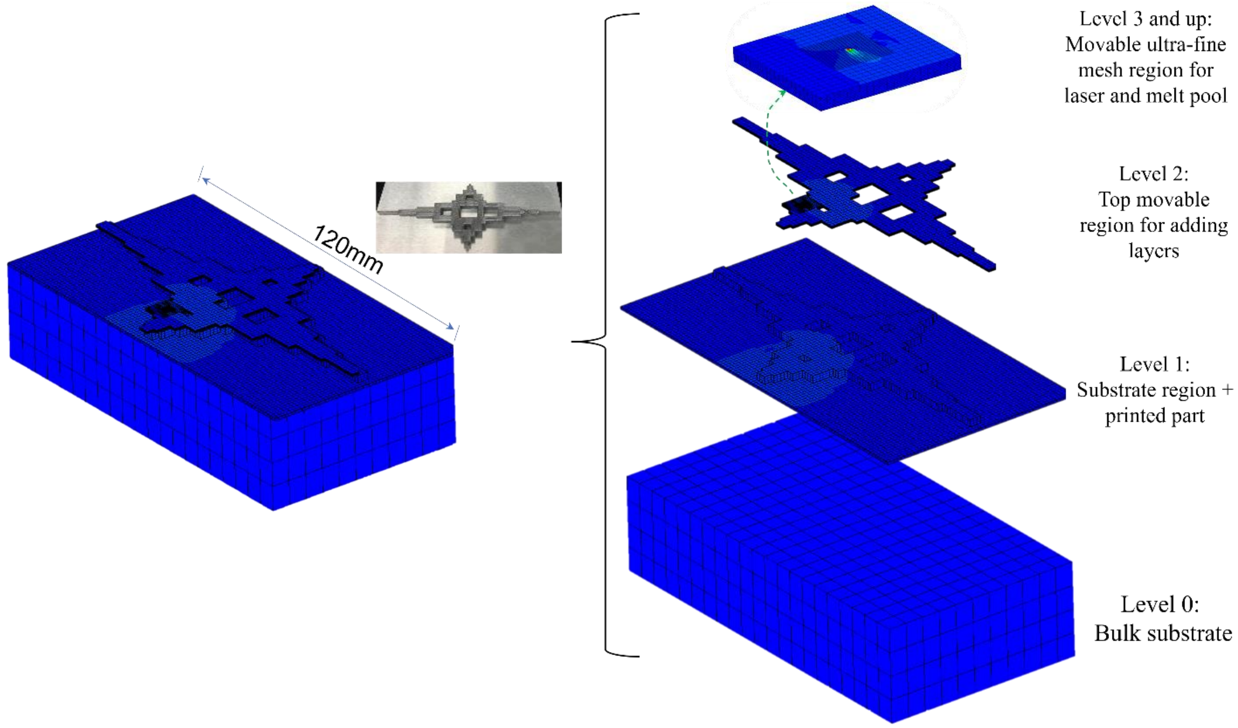

Figure 29. MUST-FE model 5-level structure for X-Y Asymmetry Demo-samples

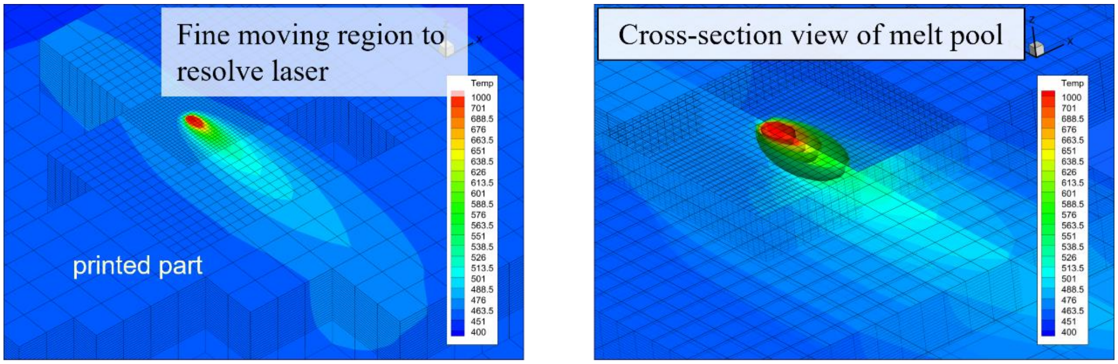

(a) (b)

Figure 30. temperature distribution and melt pool shape during MUST-FE simulation for X-Y sample.

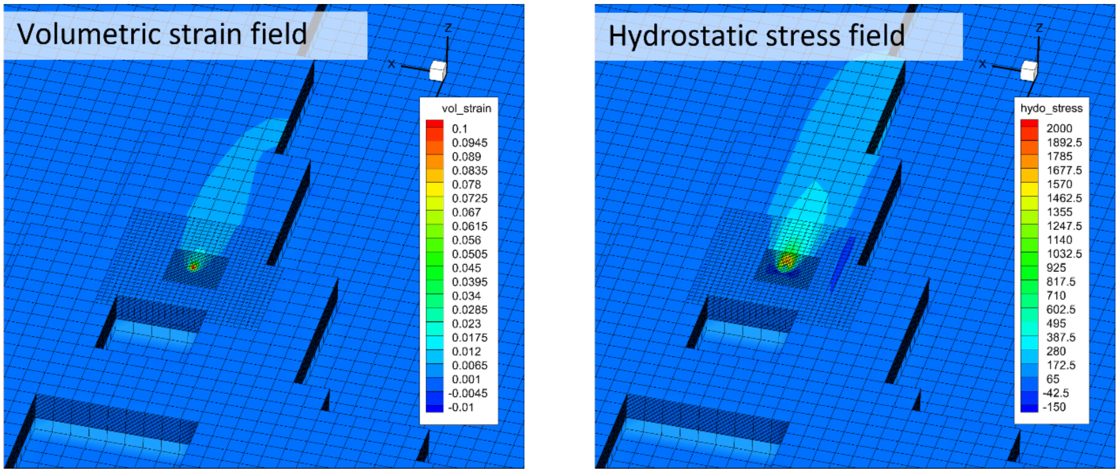

(a) (b)

Figure 31. volumetric strain field and hydrostatic stress field during MUST-FE simulation for X-Y sample.

4.4. Print X-Y Asymmetric Demo-samples using Selected Process Parameters and Characterize Residual Stress and Distortion for Model Validation at part Scale.

The X-Y Asymmetric Demo-samples are printed using AlSi10Mg powder by a SLM125 3D printer at Ford, as shown in Figure 28. The residual stress is measured using co-source x-ray diffraction at six spots in the sample as shown in Figure 31, with a resolution of beam diameter of 1mm and X-ray penetration depth 10 um. After the x-ray diffraction, the samples are removed through cutting the substrate base and the residual stress components σ_{xx} and σ_{yy}, along longitude and transverse directions respectively, are measured at six locations as shown in Figure 32. The comparison of residual stress between the simulation and experiment is shown in Figure 36a and discussed in the following sections.

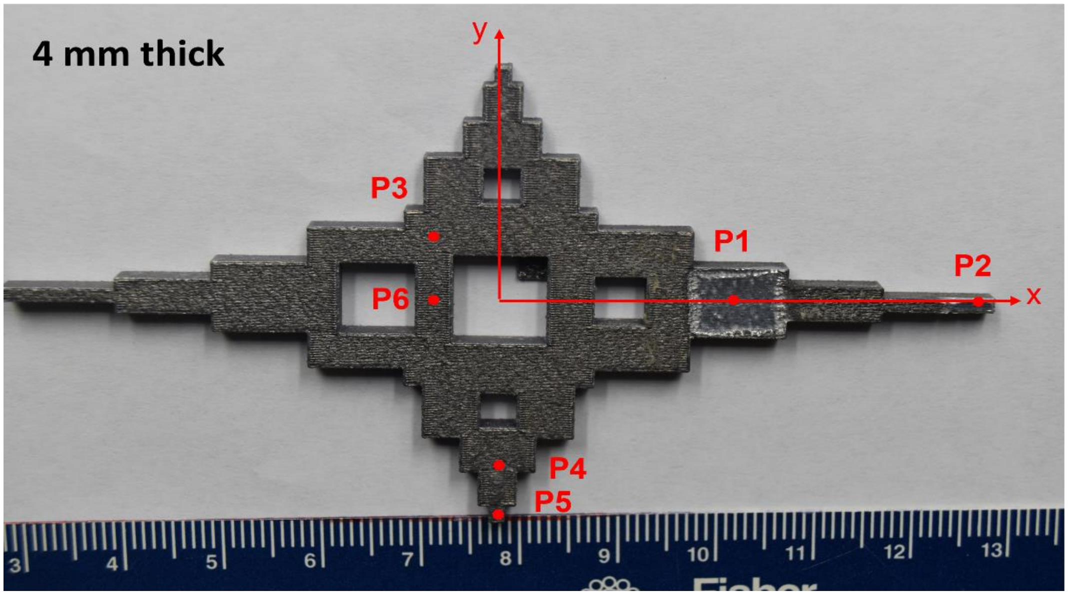

Figure 32. Schematic showing six locations for measuring residual stress with X-ray. The location of P1 is etched in the 3 directions for residual stress measurement.

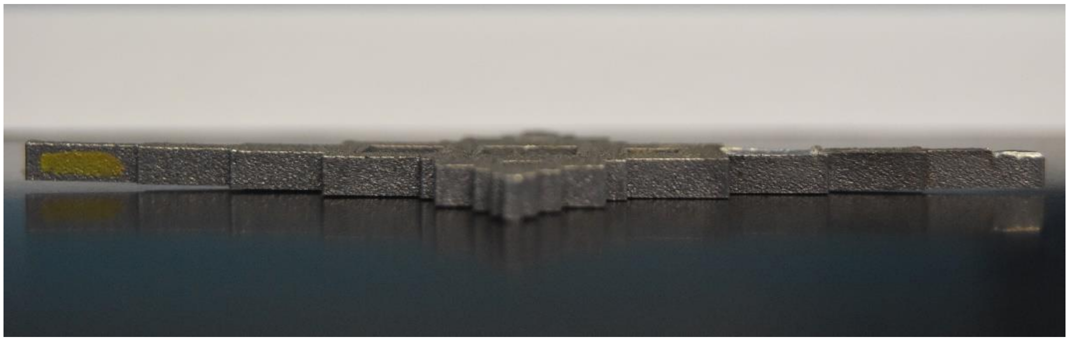

Figure 33. Distortion of the sample after cutting from the substrate base.

4.5 Benchmark and Component Demonstration

For benchmarking of the MUST-FE code, the X-Y asymmetric demo-sample is printed with multiple different scan strategies by varying the printing direction, rotation angle and laser parameters. The simulations are conducted for three scan strategies which are listed in table 3. The different scan strategies resulted to different level of residual stress and thermal distortion, which serves as benchmarking tests for MUST-FE code. The MUST-FE code, calibrated based on the residual stress measurement in section 4.4 is used to simulate the X-Y asymmetric demo-samples with different scan strategies. Each MUST-FE simulation takes ~2.25 hours to simulate one layer (containing about 400-1500 tracks depending on the scanning strategy), which is very efficient considering the large sample size and fine laser resolution.

The formation of residual stress is significantly affected by (1) the geometry of the printed part, especially the boundary constrains and the traction-free edges, and (2) the strain history or strain path. Therefore, the different scan path will inevitably lead to different residual stress distribution. Figures 34 and 35 examine the thermal stress formation during printing each layer using different scan strategies. Here, since the sample distortion is mainly along longitude direction, as shown in figure 33, we focus on the longitude stress component when examining the stress from simulation results. In figure 34 (corresponds to sample 1) the laser scan direction is parallel to longitude direction of the sample and does not change direction at each layer. This scan direction leads to a concentration of the thermal stress at the two short "arms" in the transverse direction. As the following layers repeats the same scan strategies, the residual stress accumulates at the same location. In contrast, the second sample is printed by applying a 67-degree scan angle rotation at each layer, as shown in figure 35. While the first scan is near parallel to longitude direction and causes concentration of residual stress at the two short "arms", the laser direction in the next layer is rotated to near transverse direction, and causes thermal stress concentration at the two long "arms" in the longitude direction. The change of thermal stress concentration spots at each layer avoids the concentration of residual stress at the same location, as shown in figure 35. In the 3rd examined layer, the laser direction is further rotated to between longitude and transverse direction, and no significant concentration of thermal stress is formed in this layer. Figure 36 compares the residual stress at the six spots after printing each layer (measured after finishing printing each layer and before adding a new layer in model. Note that there is a ~10 seconds wait time after printing each layer and before adding and starting the next layer, and the temperature is already dispensed during this period, therefore at this moment the stress in the model is truly the "residual stress" instead of thermal stress). For sample 1, the three consequent layers have consistent stress distribution due to the repeated laser scan along longitude direction. For longitude component of residual stress (figure 36a) P5 has the lowest residual stress because it is near the Y-edge and close to the two traction-free boundaries in longitude direction, therefore it is least constrained to deformation in longitude direction. (Note that here we assume the build higher is high enough so that the constrains from the substrate is nearly negligible, so that the boundary surfaces are "traction-free"). In the rest four spots, P2 is near one traction-free boundary in longitude direction and thus has lower longitude residual stress then the other three locations. For the similar reason, The transverse component of the residual stress has lowest value at location P2 and then P5 as shown in figure 36d, because they are near two and one traction-free edges in transverse direction, respectively. The similar trends hold for the sample 2 despite of the rotation of laser print direction at each layers, as shown in figure 36b and 36e. However, the location P1, P3 and P4 are not close to boundaries and its residual stress value has more influence on laser print directions. As shown in figure 36b, the location 1 has high residual stress when the laser direction is near transverse direction, and location 3&4 has high residual stress when laser direction is near longitude direction. The rotation of laser direction avoids the accumulation of high residual stress at same spot and thus causes large thermal distortion. Figure 37 shows the residual stress distribution on surface and in-depth after print 40 layers. As expected, the sample 1 shows a residual stress accumulation near the longitude center of the sample, which in not found in sample 2. Instead, the sample 2 only exhibits a few layers with high residual stress, as shown in the higher magnification sub-figure. Interestingly, the sample 2 exhibits residual stress accumulation at the two long-arms, which is likely due to the 67-degree rotation results in many layers has a preferred laser direction.

The simulation results of the residual stress are also measured in the six spots for the third case, which also applies a 67-degree laser direction rotation but uses a larger layer thickness. This leads to a consistent trend as sample 2 but a generally lower residual stress magnitude, as shown in figure 36c and 36f. The concentration of residual stress in longitude direction at the center of the sample 1 is likely to cause larger thermal distortion after cutting the sample from the substrate than sample 2 and 3, which is consistent with the experiment observation.

Table 3. Scan strategies for X-Y cross sample

Sample	**Laser Power (W)**	**Scan Speed (mm/s)**	**Layer Thickness (um)**	**Hatch Space (mm)**	**Scan Strategy**
1	350	1650	30	0.13	0-degree rotation angle. Bidirectional scan. No jumping around.
2	350	1650	30	0.13	67-degree rotation angle. Bidirectional scan. No Jumping around.
3	350	1650	60	0.13	67-degree rotation angle. Bidirectional scan. No Jumping around.

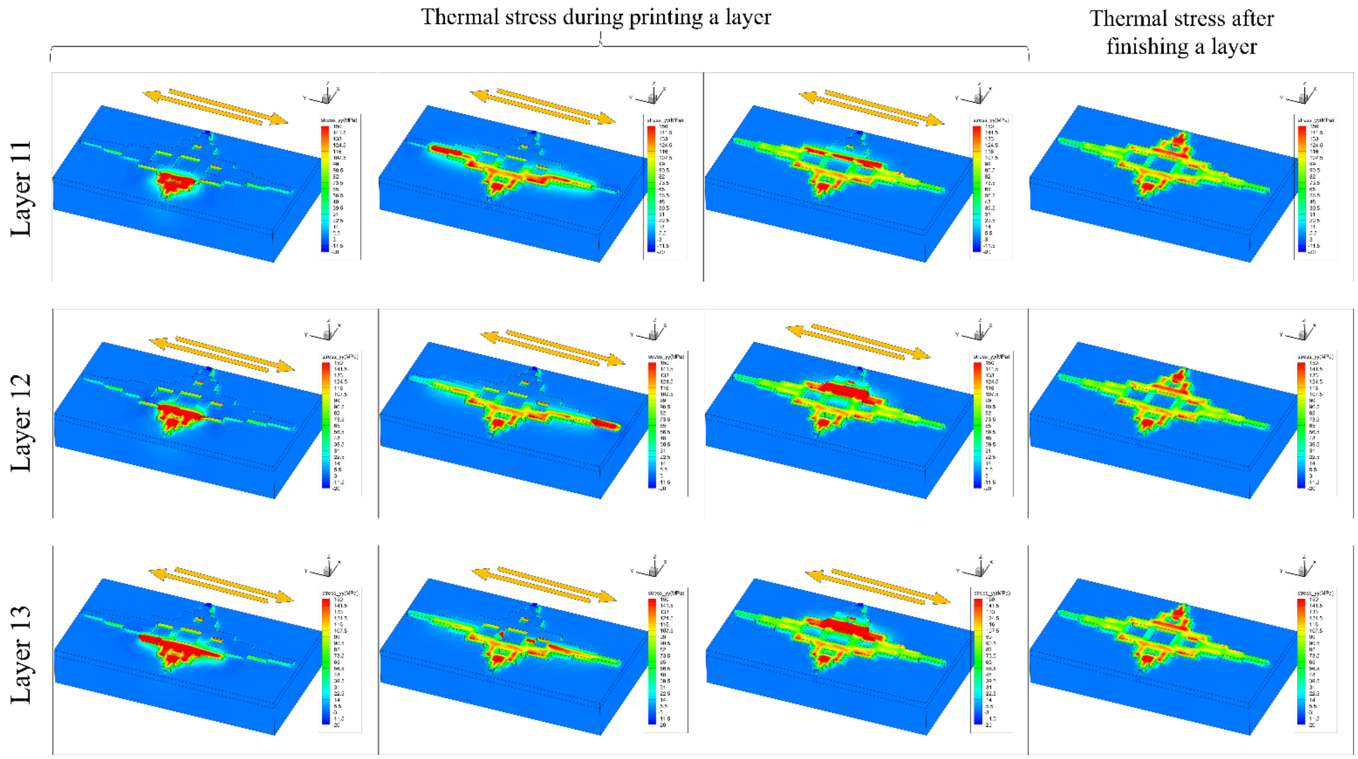

Figure 35. Simulation predicted thermal stress formation process during printing three consequent layers of sample 1.

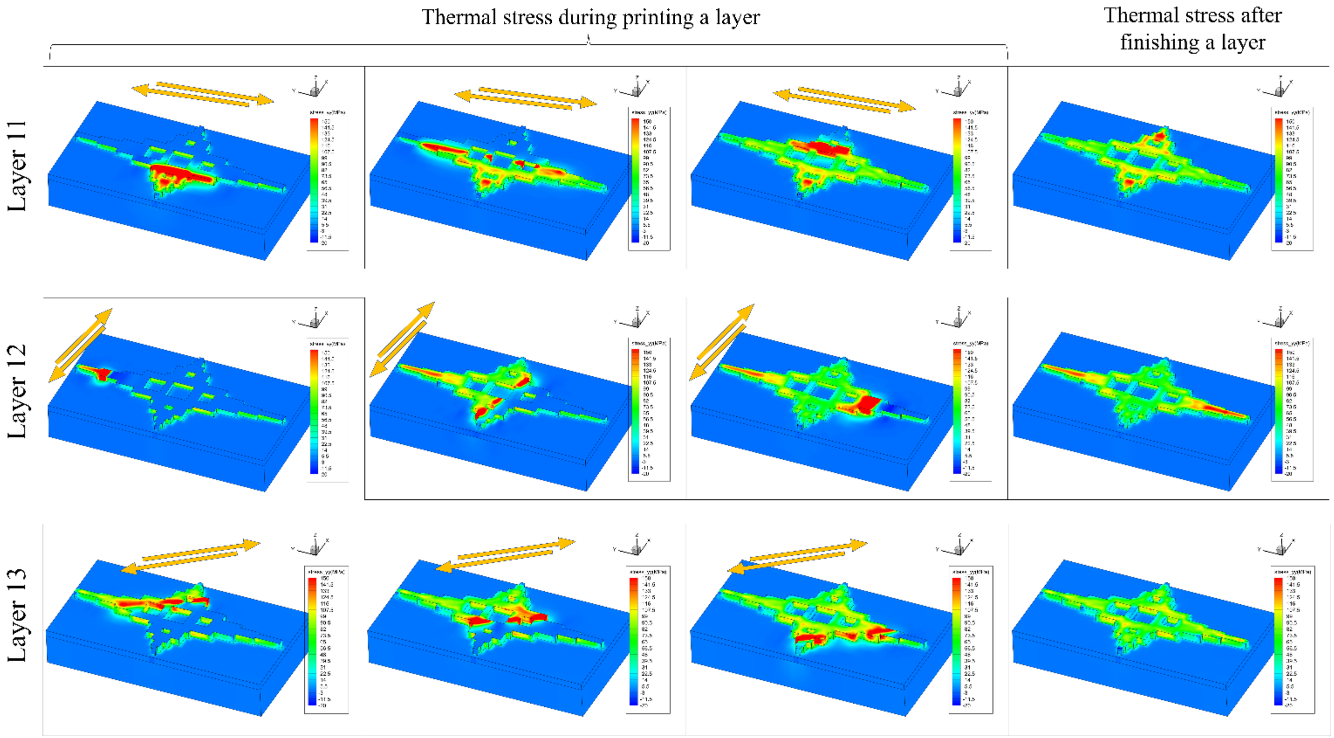

Figure 35. Simulation predicted thermal stress formation process during printing three consequent layers of sample 2.

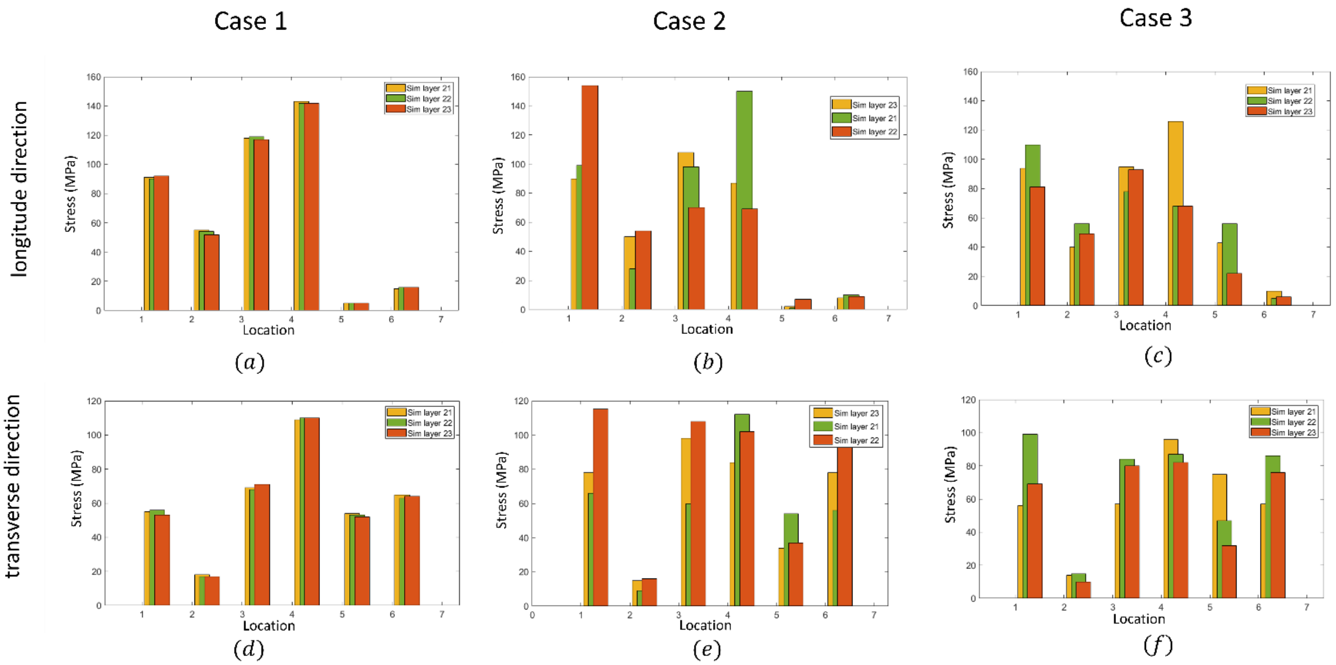

Figure 36. simulation predicted residual stress at six detection locations (see figure 32) in three samples.

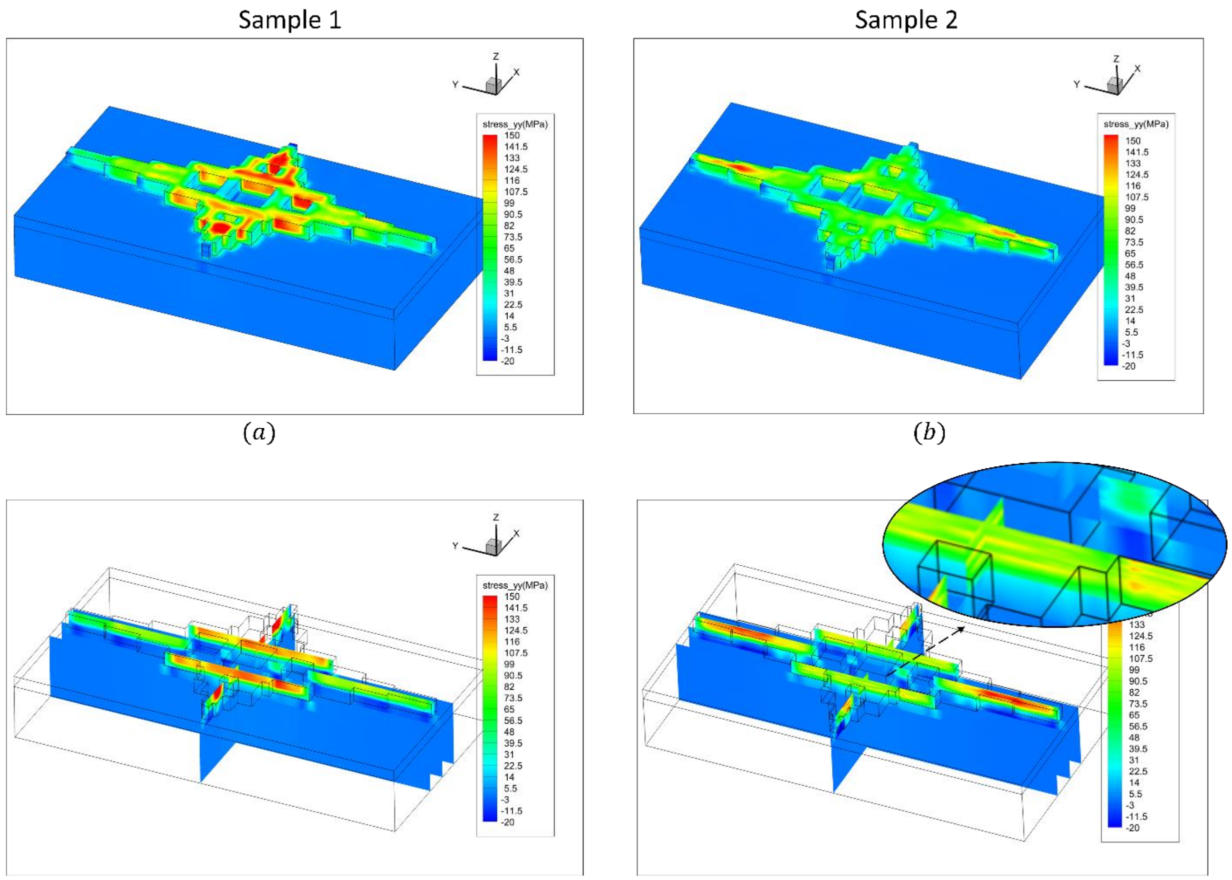

(a) (b)

(c) (d)

Figure 36. Distribution of residual stress (longitude component) in sample 1 and sample 3 at surface and in-depth.

Finally, the residual stress data measured at printed part surface are compared between the experiment and simulation for all three samples, as shown in figure 37. The simulation generally captured the pattern of residual stress distribution well. The following trends are consistent between simulation and experiments: (1) the predicted residual stress magnitude is very close to experiment measured value in all cases, (2) the residual stress in short arm direction is lower than in long direction, (3) the larger powder layer thickness leads to reduction in residual stress, (4) the simulation predicted the same distribution trend of residual stress magnitude in most locations. It is further noted the simulation captures the transverse component of the residual stress very well in all three cases, as shown in figure 37b, 37d and 37f. The longitude component of predicted residual stress generally matches with the experiment but with the exception of spot P6. Overall, the benchmark results proved the MUST-FE can be applied for reliable and efficient prediction of L-PBF process.

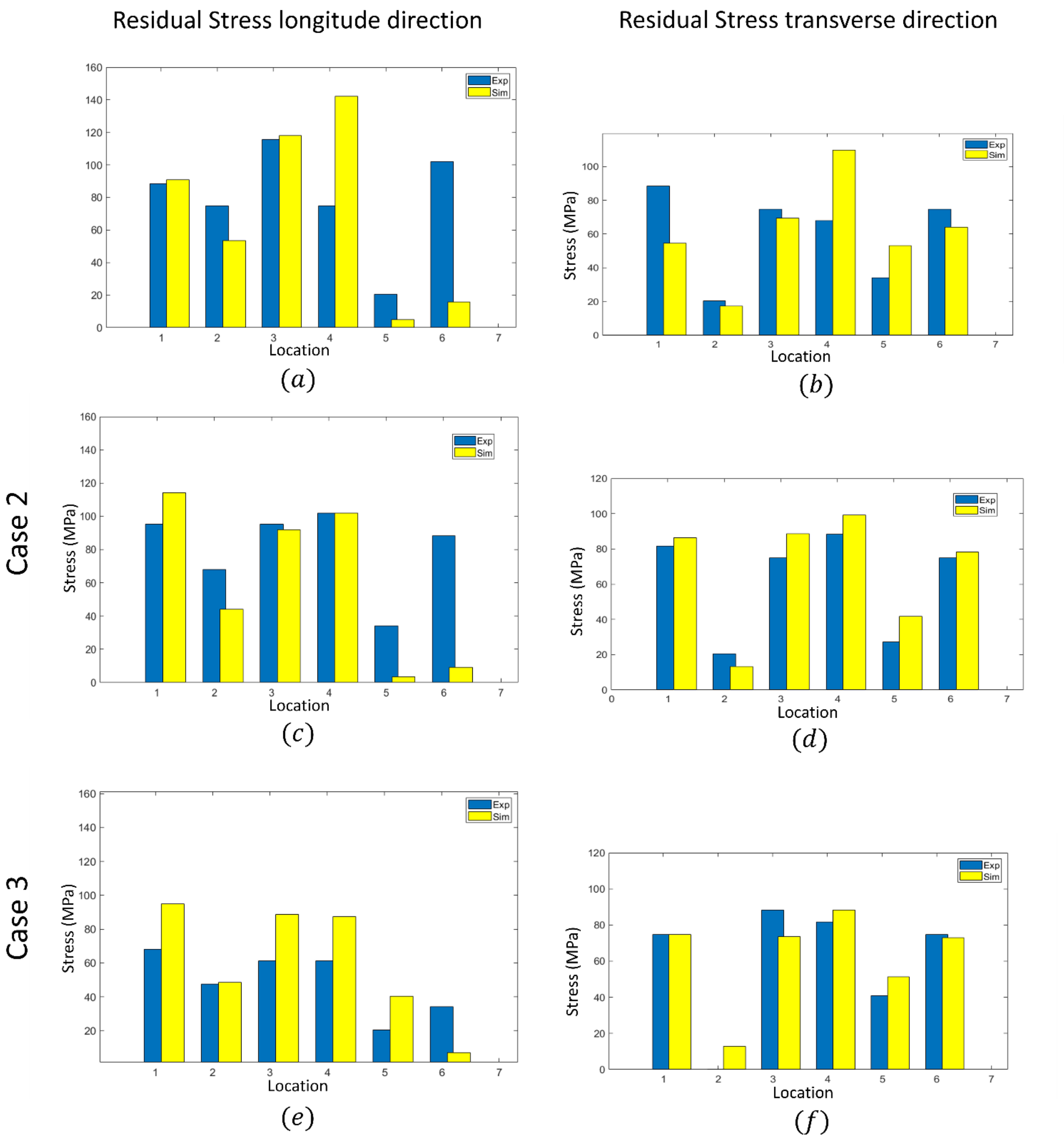

Figure 37. Comparing the simulation-predicted residual stress and the x-ray measured results in all three sample.

5.0 Subject Inventions

No subject inventions were created as part of this CRADA.

6.0 Commercialization Possibilities

The three-dimensional MUST-FE model for LBP-AM process developed in this project is built into an Fortran-based code, which will be commercialized and apply for license, then will be employed regularly for powder-bed fusion based additive manufacturing and designs in automotive and other energy industries. The code is lightweight and only requires external free package PETSC for full execution, both the MUST-FE code and PETSC can be installed on both high performance cluster platform and desktop computers. The MUST-FE code provides 1-2 order higher computation efficiency than current mesh-refinement based FE models and commercial codes, which is a valuable design tool and is implemented for commercial development use at Ford.

7.0 Plans for Future Collaboration

Ford Motor Company appreciate the support from Department of Energy, advanced manufacturing office for supporting this project. This project fostered a new connection between the Ford Motor Company and Oak Ridge National Laboratory Energy & Manufacturing Science Division. The Oak Ridge National Laboratory team provided outstanding technical expertise and value to Ford during this program. The Ford and Oak Ridge teams will continue work on commercialization of the MUST-FE code and applying the code to address remaining technical challenges in powder-bed fusion based additive manufacturing process.

8.0 Conclusions

Powder bed fusion-additive manufacturing (PBF-AM) is free from traditional metal manufacturing constraints and enables fast fabrication of highly complex and integrated structures, showing promises in advanced manufacturing of multi-functional material and light-weighting. However, the geometric complexity of PBF-AM technique also leads to highly non-uniform heating and cooling rate in the printed part, which may cause flaw formation and increase quality uncertainties and manufacture issues, leading to increases in cost and energy consumption in the form of rejected parts. It is very challenging to optimize the process parameters solely based on empirical testing especially for explorative designs, and the utilization of high-fidelity computing models can significantly reduce the uncertainty in the experiments and helps to improve the PBF-AM process design. However, the conventional thermal-mechanical finite element (FE) method applied to part-scale PBF-AM process has suffered from tremendous computational cost and simulation time. Direct FE simulation is impossible because of (1) the large difference between the length scale of the actual part and the length scale of the fine laser/electron beam track and powder layer thickness, and (2) the large number of tracks to be simulated. Adaptive refinement algorithms or hierarchical FE formulation has been developed to alleviate the computation cost, but the improved simulation time is still beyond an acceptable range. The mostly adopted and practical part-scale FE simulation methods are based on using coarse mesh and taking compromises by either grouping multiple tracks and/or layers together, or by conducting fine-resolution simulations for limited tracks and use interpolation, which both sacrifice the prediction accuracy.

In this project, we developed a novel MUST-FE formulation for direct simulation of part-scale PBF-AM process which not only provide high computation speed but also reserves fine resolution for meltpool profile and residual stress predictions. The MUST-FE method starts by constructing multi-levels overlapping sub-domains with different FE mesh resolution, and the holistic part simulation is accordingly decomposed into multiple separate sub-domain FE simulations which iteratively transfers boundary thermal profiles and heat flux to keep synchronized. The thermal and mechanical fields are staggerly coupled in the MUST-FE framework. The high resolution temperature field, plastic strain and residual stress are predicted by MUST-FE model during the layer-by-layer laser scanning process, which provides physics insight to PBF-AM process which is experimental unmeasurable. The MUST-FE method is 1-2 order faster than other mesh-refinement based FE methods. The reduction in computation cost and simulation time is achieved by (1) avoiding adaptive remeshing and changing connectivity, (2) breaking the holistic sparse matrix into several smaller sparse matrixes, (3) different sub-domains are solved using different time increments. The proposed model and method are thus expected to improve the reliability of FE simulations, leading to higher accuracy designing tool for complex L-PBF process. The MUST-FE code will be commercialized by apply for license and become ready for open industrial utilization.

9.0 References

[1] C. Li, J.F. Liu, X.Y. Fang, Y.B. Guo, Efficient predictive model of part distortion and residual stress in selective laser melting, Addit. Manuf. 17 (2017) 157–168. https://doi.org/10.1016/j.addma.2017.08.014.

[2] N. Raghavan, R. Dehoff, S. Pannala, S. Simunovic, M. Kirka, J. Turner, N. Carlson, S.S. Babu, Numerical modeling of heat-transfer and the influence of process parameters on tailoring the grain morphology of IN718 in electron beam additive manufacturing, Acta Mater. 112 (2016) 303–314. https://doi.org/10.1016/j.actamat.2016.03.063.

[3] D.C. Weckman, H.W. Kerr, J.T. Liu, The effects of process variables on pulsed Nd:YAG laser spot welds: Part II. AA 1100 aluminum and comparison to AISI 409 stainless steel, Metall. Mater. Trans. B Process Metall. Mater. Process. Sci. 28 (1997) 687–700. https://doi.org/10.1007/s11663-997-0043-1.

[4] W.E. King, H.D. Barth, V.M. Castillo, G.F. Gallegos, J.W. Gibbs, D.E. Hahn, C. Kamath, A.M. Rubenchik, Observation of keyhole-mode laser melting in laser powder-bed fusion additive manufacturing, J. Mater. Process. Technol. 214 (2014). https://doi.org/10.1016/j.jmatprotec.2014.06.005.

[5] J. Goldak, A. Chakravarti, M. Bibby, A new finite element model for welding heat sources, Metall. Trans. B. 15 (1984). https://doi.org/10.1007/BF02667333.

[6] S. Shrestha, Y. Kevin Chou, A Numerical Study on the Keyhole Formation During Laser Powder Bed Fusion Process, J. Manuf. Sci. Eng. 141 (2019) 1–9. https://doi.org/10.1115/1.4044100.

[7] M. Plumlee, V.R. Joseph, H. Yang, Calibrating functional parameters in the ion channel models of cardiac cells, J. Am. Stat. Assoc. 111 (2016) 500–509.

[8] V.R. Joseph, E. Gul, S. Ba, Maximum projection designs for computer experiments, Biometrika. 102 (2015) 371–380.

[9] D. Foreman-Mackey, D.W. Hogg, D. Lang, J. Goodman, emcee: the MCMC hammer, Publ. Astron. Soc. Pacific. 125 (2013) 306.

[10] S. Conti, A. O'Hagan, Bayesian emulation of complex multi-output and dynamic computer models, J. Stat. Plan. Inference. 140 (2010) 640–651.